



Invited review article

Markers of the pyroxenite contribution in the major-element compositions of oceanic basalts: Review of the experimental constraints

Sarah Lambart ^a, Didier Laporte ^{b,c}, Pierre Schiano ^{b,c}

^a Division of Geological and Planetary Sciences 170-25, California Institute of Technology, Pasadena, CA 91125, USA

^b Laboratoire Magmas et Volcans, Clermont Université, Université Blaise Pascal, BP 10448, 63000 Clermont-Ferrand, France

^c CNRS, UMR 6524, IRD, R 163, 5 rue Kessler, F-63038 Clermont-Ferrand Cedex, France

ARTICLE INFO

Article history:

Received 27 August 2012

Accepted 17 November 2012

Available online 24 November 2012

Keywords:

Experimental petrology

Pyroxenite

Thermal divide

Oceanic basalts

Partial melting

Melt–peridotite interactions

ABSTRACT

Based on previous and new results on partial melting experiments of pyroxenites at high pressure, we attempt to identify the major element signature of pyroxenite partial melts and to evaluate to what extent this signature can be transmitted to the basalts erupted at oceanic islands and mid-ocean ridges. Although peridotite is the dominant source lithology in the Earth's upper mantle, the ubiquity of pyroxenites in mantle xenoliths and in ultramafic massifs, and the isotopic and trace elements variability of oceanic basalts suggest that these lithologies could significantly contribute to the generation of basaltic magmas. The question is how and to what degree the melting of pyroxenites can impact the major-element composition of oceanic basalts. The review of experimental phase equilibria of pyroxenites shows that the thermal divide, defined by the aluminous pyroxene plane, separates silica-excess pyroxenites (SE pyroxenites) on the right side and silica-deficient pyroxenites (SD pyroxenites) on the left side. It therefore controls the melting phase relations of pyroxenites at high pressure but, the pressure at which the thermal divide becomes effective, depends on the bulk composition; partial melt compositions of pyroxenites are strongly influenced by non-CMAS elements (especially FeO, TiO₂, Na₂O and K₂O) and show a progressive transition from the liquids derived from the most silica-deficient compositions to those derived from the most silica-excess compositions. Another important aspect for the identification of source lithology is that, at identical pressure and temperature conditions, many pyroxenites produce melts that are quite similar to peridotite-derived melts, making the determination of the presence of pyroxenite in the source regions of oceanic basalts difficult; only pyroxenites able to produce melts with low SiO₂ and high FeO contents can be identified on the basis of the major-element compositions of basalts. In the case of oceanic island basalts, high CaO/Al₂O₃ ratios can also reveal the presence of pyroxenite in the source-regions. Experimental and thermodynamical observations also suggest that the interactions between pyroxenite-derived melts and host peridotites play a crucial role in the genesis of oceanic basalts by generating a wide range of pyroxenites in the upper mantle: partial melting of such secondary pyroxenites is able to reproduce the features of primitive basalts, especially their high MgO contents, and to impart, at least in some cases, the major-element signature of the original pyroxenite melt to the oceanic basalts. Finally, we highlight that the fact the very silica depleted compositions (SiO₂ < 42 wt.%) and high TiO₂ contents of some oceanic island basalts seem to require the contribution of fluids (CO₂ or H₂O) through melting of either carbonated lithologies (peridotite or pyroxenite) or amphibole-rich veins.

© 2012 Elsevier B.V. All rights reserved.

Contents

1. Introduction	15
2. Garnet–pyroxene thermal divide and compositional variability of pyroxenite melts	15
2.1. Constraints on the effective pressure of the garnet–pyroxene thermal divide	16
2.1.1. The CMAS (CaO–MgO–Al ₂ O ₃ –SiO ₂) system	16
2.1.2. From CMAS to natural systems: modeling the effects of FeO, Na ₂ O, K ₂ O and TiO ₂	17

Corresponding author at: California Institute of Technology, MC 170-25, Pasadena, CA 91125, USA. Tel.: +1 626 240 9705; fax: +1 626 568 0935.

E-mail address: slambart@caltech.edu (S. Lambart).

2.2.	Melt composition variability	21
2.2.1.	Melts compositions and thermal divide	21
2.2.2.	Melts compositions at pressures <2 GPa	22
2.2.3.	The effect of fluids	22
3.	Pyroxenites in oceanic basalt genesis	23
3.1.	Pyroxenites in MORB source-regions	25
3.1.1.	SiO ₂ and FeO: barometers and/or markers of the pyroxenite contribution?	25
3.1.2.	Quantification of the role of pyroxenites	26
3.2.	Pyroxenites in OIB source-regions	27
3.2.1.	Pyroxenite versus peridotite major-element signatures	27
3.2.2.	Implications for mantle melting beneath Hawaii during the post-shield phase	28
3.3.	Preservation of the pyroxenite signal during melt extraction and transport	30
3.4.	Importance of pyroxenite–peridotite interactions in the genesis of oceanic basalts	31
3.4.1.	Direct interaction model	31
3.4.2.	Indirect interaction model: formation of stage 2 pyroxenites from SE and SD pyroxenite-derived melts	31
3.5.	Nature of pyroxenites in the source of oceanic basalts and the origin of SD pyroxenites	32
4.	Summary points	33
	Acknowledgements	33
	References	34

1. Introduction

The petrogenesis and differentiation processes of mantle-derived magmas have been the subject of numerous studies both direct (i.e., experimental melting of ultramafic rocks) and indirect via the study of lavas, and are now reasonably well characterized. Accordingly, partial melting of a peridotitic-type mantle, melt extraction and ascent, fractional crystallization, and potentially crustal contamination are thought to be responsible for the genesis of various types of mafic magmas, such as mid-ocean ridge basalts (MORB), ocean island basalts (OIB), and volcanic arc basalts (e.g., McKenzie and Bickle, 1988). Understanding of these processes has reached a reasonably mature state, thanks to numerous experiments (e.g., Baker et al., 1995; Davis et al., 2011; Falloon et al., 2008; Green and Ringwood, 1967; Kushiro, 1969; O'Hara, 1968; Presnall et al., 1978; Presnall et al., 2002; Stolper, 1980; Takahashi and Kushiro, 1983; Walker et al., 1979; Yoder and Tilley, 1962) and theoretical studies (e.g., Asimow et al., 2001; Grove et al., 1992; Kinzler and Grove, 1992a,b; Klein and Langmuir, 1987; Langmuir et al., 1992; Niu and Batiza, 1997; Niu et al., 2011; Plank and Langmuir, 1992; Stolper and Asimow, 2007).

However, the compositional variability of oceanic lavas cannot be generated by varying the melting degree of peridotite, and thus suggests strong lithological heterogeneities in the source of these magmas (e.g., Hanson, 1977; Wood, 1979; Zindler et al., 1984), which are corroborated by the observed isotopic variations (e.g., Allègre and Turcotte, 1986; White, 1985; Zindler and Hart, 1986). Therefore, several authors have proposed that olivine-poor lithologies such as pyroxenites and eclogites contribute significantly to the generation of basaltic magmas (e.g., Chase, 1981; Helffrich and Wood, 2001; Hirschmann and Stolper, 1996; Hofmann, 1997; Hofmann and White, 1982; Salters and Dick, 2002; Schiano et al., 1997). The source of basalts is therefore now envisioned as a heterogeneous mantle that comprises a range of lithological heterogeneities, especially pyroxenites, introduced into peridotites by various geodynamic and magmatic processes. Consequently, many experimental studies in the last two decades have sought to constrain the melting relations and partial melt compositions of pyroxenites, and to discuss their role in basalt genesis. The starting compositions used in these studies are compared to natural pyroxenite compositions in Figs. 1 and 2 (the compositions of starting materials used in experimental studies of pyroxenite partial melting are summarized in Table S1 in the supplementary material).

The significance of pyroxenitic rocks in basalt source regions is still widely debated. Geochemical evidence has been used to argue

for, or against, an important role of pyroxenites in various localities (e.g., Day et al., 2009; Hékinian et al., 2000; Herzberg, 2006, 2011; Michael et al., 2003; Salters and Dick, 2002; Sobolev et al., 2005, 2007; Stracke and Bourdon, 2009; Stracke et al., 1999), and the potential effect of these lithologies on the major-element variability of oceanic basalts remains unclear (Hauri, 1996; Humphreys and Niu, 2009; Korenaga and Kelemen, 2000; Le Roux et al., 2002; Niu et al., 2011; Shorttle and MacLennan, 2011). This work aims to identify potential markers of pyroxenite contribution in the major-element compositions of oceanic basalts. With this objective in mind, we start by reviewing experimental phase equilibria of pyroxenites, both in simple systems and in natural compositions, to provide strong constraints on the relationships between bulk compositions, melt compositions, and the pressure (P)–temperature (T) conditions of magma formation (beneath oceanic islands and mid-ocean ridges). We then evaluate to what extent the characteristic major-element features of pyroxenite-derived melts are reflected in the basalts erupted at the Earth's surface.

2. Garnet–pyroxene thermal divide and compositional variability of pyroxenite melts

Kogiso et al. (2004a) provided a detailed review of the phase relations of pyroxenites at high pressures. In particular, they emphasized the potential influence of the thermal barrier defined by the aluminous-pyroxene plane, on melt compositions (Fig. 2a). In the pseudoternary diagram forsterite (Fo)–Ca-Tschermak's pyroxene (CaTs)–quartz (Qz) projected from diopside (Di), the thermal divide is defined by the enstatite (En)–CaTs join (Fig. 2b). Because all stoichiometric garnets and pyroxenes project along the En–CaTs join, when these two minerals are the major phases in the residue, the divide is stable and separates two fundamental types of pyroxenites (Kogiso et al., 2004a; Schiano et al., 2000): silica-excess pyroxenites on the right side and silica-deficient pyroxenites on the left side (termed respectively SE and SD pyroxenites hereafter) and thus, melting and crystallization paths of compositions on opposite sides of this join diverge.

Despite the critical influence of this thermal divide on the melting relations of pyroxenites, the significance of its influence, in terms of pressure and composition, has not been precisely determined and its effects on melt compositions, especially at low fractions, are not well established. Consequently, based on previous and new experimental data, we start by constraining the extent of this thermal divide and its influence on melt compositions.

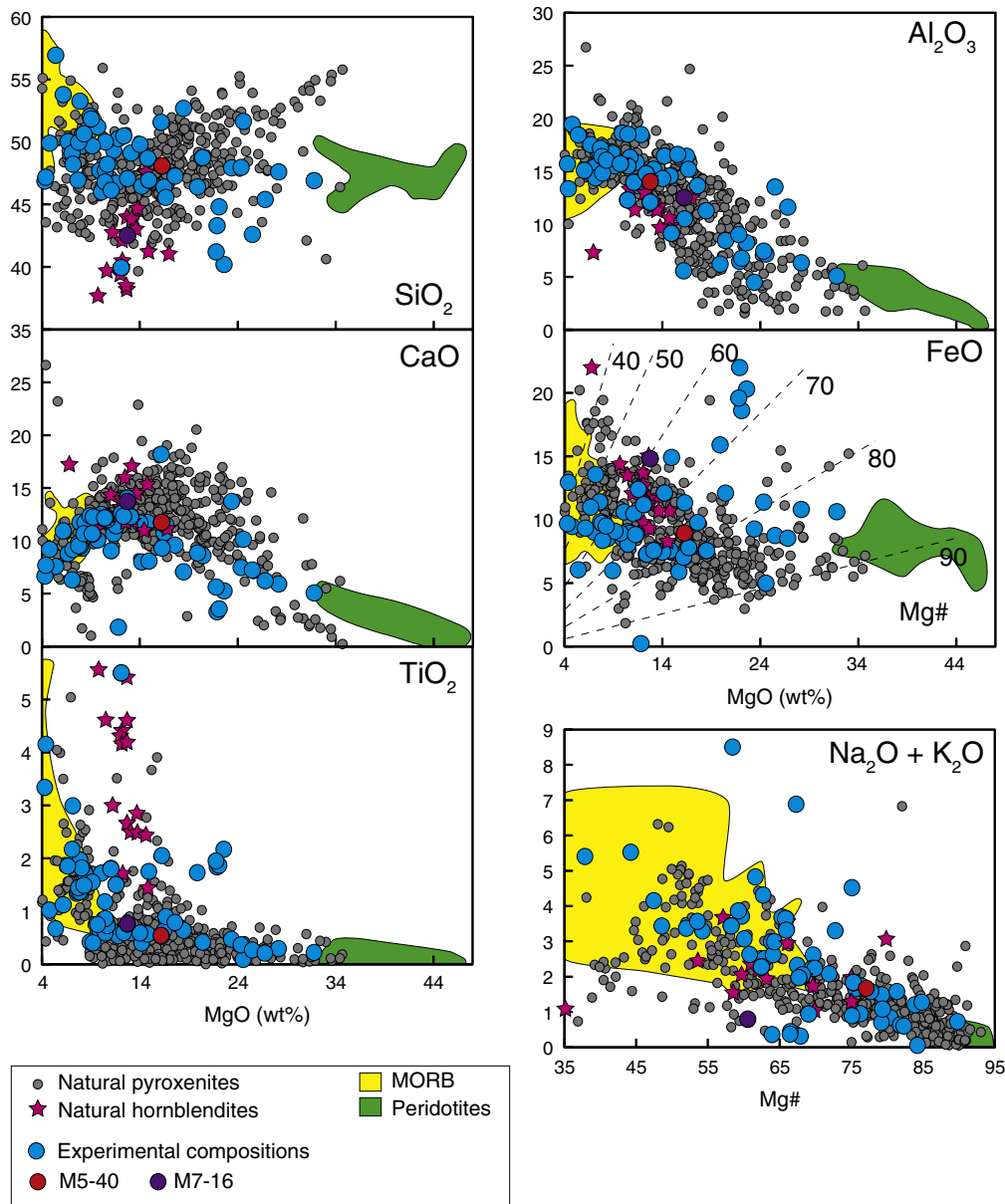


Fig. 1. Oxide contents (in wt.%) and Mg# of natural pyroxenites (small gray circles, Lambert et al., 2009 and references within) and hornblendites (pink stars, Arculus et al., 1983; Ho et al., 2000; Moine et al., 2000; Neumann et al., 1999; Orejana et al., 2006; Pilet, personal communication) from xenoliths and alpine-type massifs compared to starting compositions in experimental studies (large circles, Table S1). Pyroxenites M5-40 and M7-16 used as starting materials in this study are represented by the red and purple circles, respectively. Also shown are the fields of mantle peridotites from GEOROC database (green area, <http://georoc.mpch-mainz.gwdg.de>) and MORB matrix glasses (yellow area, Melson and O'Hearn, 2003).

2.1. Constraints on the effective pressure of the garnet–pyroxene thermal divide

2.1.1. The CMAS (CaO–MgO–Al₂O₃–SiO₂) system

In the following section, we review the liquidus phase relations in simple systems in order to identify the influence of each component on the thermal barrier. The aluminous pyroxene plane was identified as a high pressure thermal divide by O'Hara and Yoder (1963) with regard to pyroxene and/or garnet crystallization. They observed that at high pressure, the forsterite primary phase volume lies on the SiO₂-poor side of the plane and melts produced by a garnet lherzolite are trapped behind this plane. Subsequent papers (Kushiro and Yoder, 1974; Maaløe and Wyllie, 1979; O'Hara and Yoder, 1967; O'Hara, 1965, 1968, 1969a,b) further discussed this issue and provided additional data to clarify the relevant phase relations.

The pressure at which the thermal divide becomes effective, is the pressure at which the phase volume of garnet (Gt) intersects the aluminous pyroxene plane, or, in other words, when the melt in equilibrium with clinopyroxene (Cpx), orthopyroxene (Opx), Gt, spinel (Sp), and potentially olivine (Ol), is on the SiO₂-poor side of the aluminous pyroxene plane (i.e., on the left side of the En–CaTs join in Fig. 2b). Based on available experimental data, Kushiro and Yoder (1974) suggested that the plane becomes a thermal divide at one pressure between 2.6 and 3 GPa. More recently Milholland and Presnall (1998) have located the invariant point at 3 GPa slightly on the low-SiO₂ side, increasing the pressure at which the thermal divide becomes effective up to a pressure very close to 3 GPa.

Note that if the phase volume of a mineral other than pyroxene and Gt intersects the aluminous plane, the plane no longer behaves as a thermal divide for compositions in this phase volume. In the CMAS system, Sp is the only phase in this category.

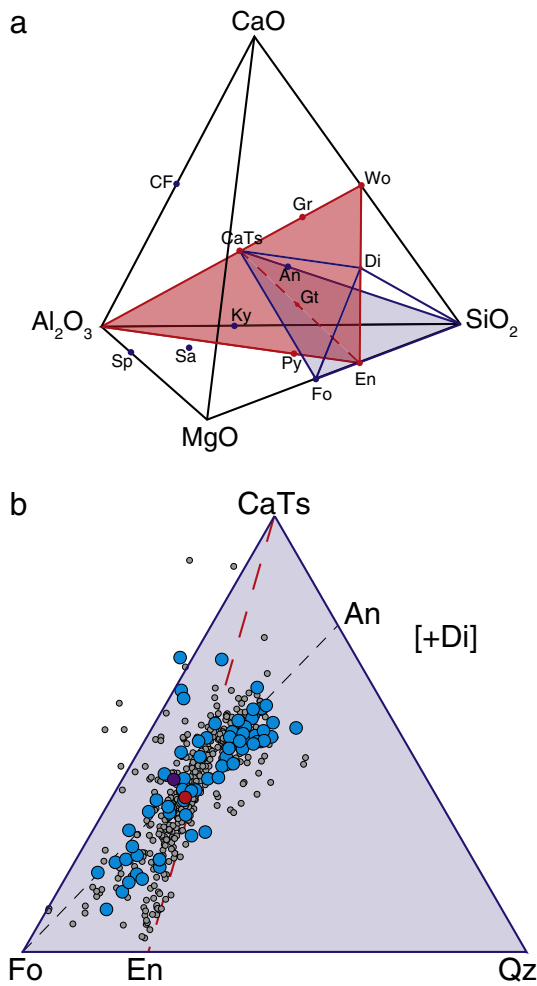


Fig. 2. (a) Representation of the aluminous pyroxene plane $\text{MgSiO}_3\text{-CaSiO}_3\text{-Al}_2\text{O}_3$ (in red) in the tetrahedron $\text{CaO-MgO-Al}_2\text{O}_3\text{-SiO}_2$. (b) Molecular normative projection of natural pyroxenites (small gray circles) and of starting materials in experimental studies (large circles) from Di on the pseudoternary system Fo-CaTs-Qz [the blue plane in (a)], using the method of O'Hara (1972). The red and the purple circles represent the pyroxenites M5-40 and M7-16, respectively. Nepheline- (Ne-) and hypersthene- (Hy-) normative compositions are separated by the plane Di-Fo-An , the critical plane of silica undersaturation; Hy- and Ol-normative compositions are separated from the Qz-normative compositions by the silica saturation plane En-An-Di (Yoder and Tilley, 1962). According to the classification of Kogiso et al. (2004a), silica-deficient (SD) and silica-excess (SE) pyroxenites are located on the left and right sides, respectively, of the CaTs-En join (red dashed line). An, anorthite ($\text{CaAl}_2\text{Si}_2\text{O}_8$); CaTs, Ca Tschermak's molecule ($\text{CaAl}_2\text{SiO}_6$); CF, high pressure aluminous phase (CaAl_2O_4) with a calcium ferrite structure; Di, diopside ($\text{CaMgSi}_2\text{O}_6$); En, enstatite (MgSiO_3); Fo, forsterite (Mg_2SiO_4); Gt, garnet ($\text{CaMg}_2\text{Al}_2\text{Si}_2\text{O}_{12}$); Gr, grossular ($\text{Ca}_3\text{Al}_2\text{Si}_3\text{O}_{12}$); Py, pyrope ($\text{Mg}_3\text{Al}_2\text{Si}_3\text{O}_{12}$); Sp, spinel (MgAl_2O_4); Wo, wollastonite (CaSiO_3); Ky, kyanite (Al_2SiO_5); Sa, sapphirine ($\text{Mg}_2\text{Al}_4\text{SiO}_{10}$); and Qz, quartz (SiO_2).

2.1.2. From CMAS to natural systems: modeling the effects of FeO , Na_2O , K_2O and TiO_2

Experiments in the simplified CMAS system (e.g., Kushiro, 1969; Liu and Presnall, 2000; Milholland and Presnall, 1998; O'Hara and Yoder, 1967; Presnall et al., 1978) helped to define the melting relations of pyroxenites up to 3 GPa. However, to interpret natural compositions, the effect of the other major elements of mafic melts on phase relations needs to be understood: Na_2O , FeO , TiO_2 , and K_2O . We will first consider Na_2O and FeO . Walter and Presnall (1994) studied the melting relations of peridotites in the CMASN ($\text{CaO-MgO-Al}_2\text{O}_3\text{-SiO}_2\text{-Na}_2\text{O}$) system between 0.7 and 3.5 GPa, and Gudfinnsson and Presnall (2000) performed a similar study in the CMASF ($\text{CaO-MgO-Al}_2\text{O}_3\text{-SiO}_2\text{-FeO}$) system between 0.7 and 2.8 GPa. The liquidus phase relations in the CMAS system at 2 GPa (Liu and Presnall, 2000) are displayed in Fig. 3, in which point I represents the melt in equilibrium with Ol+Opx+Cpx+Sp (I is

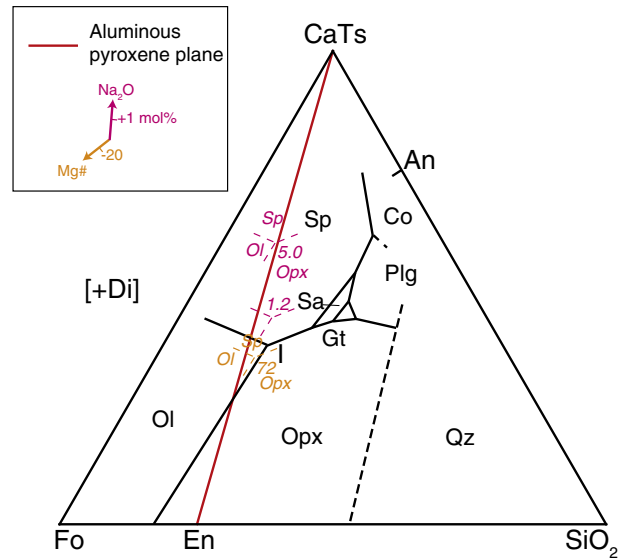


Fig. 3. Diopside saturation surface in the CMAS system projected from Di on the Fo-CaTs-Qz plane at 2 GPa based on Liu and Presnall's experimental data (2000). Point I represents the composition of melt in equilibrium with Ol, Opx, Cpx and Sp . Pink data represent the compositions of melts in equilibrium with Ol, Opx, Cpx and Sp in the CMASN system (Walter and Presnall, 1994), with their Na_2O content given in mol%. Orange point and number represent the projection and the Mg\# of melt in equilibrium with Ol, Opx, Cpx and Sp in the CMASF system (Gudfinnsson and Presnall, 2000). Linear axes $[\text{Na}_2\text{O}]$ and $[\text{Mg\#}]$ in the inset describe the displacement of point I with increasing Na_2O content in melt and with decreasing Mg\# in melt, respectively. We used the O'Hara's method (1972) for the projection. Abbreviations are as in Fig. 2.

invariant at constant pressure in the CMAS system). For comparison, we also report selected melt compositions in equilibrium with Ol+Opx+Cpx+Sp in the CMASN system (a melt with 1.2 mol% Na_2O and one with 5.0 mol%; Walter and Presnall, 1994) and in the CMASF system (a melt with $\text{Mg\#} = 72$, where Mg\# is the molar ratio $100 \times \text{Mg}^{2+} / [\text{Mg}^{2+} + \text{Fe}^{2+}]$; Gudfinnsson and Presnall, 2000).

Available experimental data suggest that: (1) with the addition of sodium oxide to the system, point I shifts away from its position in the CMAS system towards the CaTs , an effect already known at low pressure (1 atm.; Kushiro, 1975) where the addition of oxides of monovalent cations (namely, K_2O and Na_2O) causes the liquidus field of Fo to expand relative to that of En . (2) With the addition of iron oxide, point I shifts away towards the Fo . In the following, we propose a model able to reproduce the effects of the non-CMAS major-elements on phase relations. To a first approximation, we consider that the displacement of point I in the CMASN and CMASF systems occurs along a linear axis and is proportional to the molar percentage of Na_2O in the melt in the CMASN system, and to 100 minus the Mg\# of the melt in the CMASF system. The two linear axes are labeled $[\text{Na}_2\text{O}]$ and $[\text{Mg\#}]$ in Fig. 3. This linear approximation is consistent with experimental results of Walter and Presnall (1994) and Gudfinnsson and Presnall (2000).

The effects of K_2O and TiO_2 can be deduced from the experiments of Kogiso et al. (1998) on basalt-peridotite mixes KG1 and KG2. At 2 GPa, the liquids L_{KG1} and L_{KG2} , derived from KG1 and KG2 at 8 and 3% of melting, respectively, are in equilibrium with Ol, Opx, Cpx and Sp (Table S2 in the supplementary material). In Fig. 4, we project these melt compositions from Di on the plane Fo-CaTs-Qz . The differences between the position of I in the CMAS system and the positions of L_{KG1} and L_{KG2} are likely to reflect the effects of major elements other than CaO , MgO , Al_2O_3 , and SiO_2 in KG1 and KG2: namely Na_2O , FeO , TiO_2 , Cr_2O_3 , P_2O_5 and K_2O . If we subtract the effects of Na_2O and Mg\# as explained above, we obtain two residual vectors (the green arrows in Fig. 4) that embody the effects of TiO_2 , Cr_2O_3 , P_2O_5 and K_2O . KG1 and KG2 do not contain any P_2O_5 . Moreover,

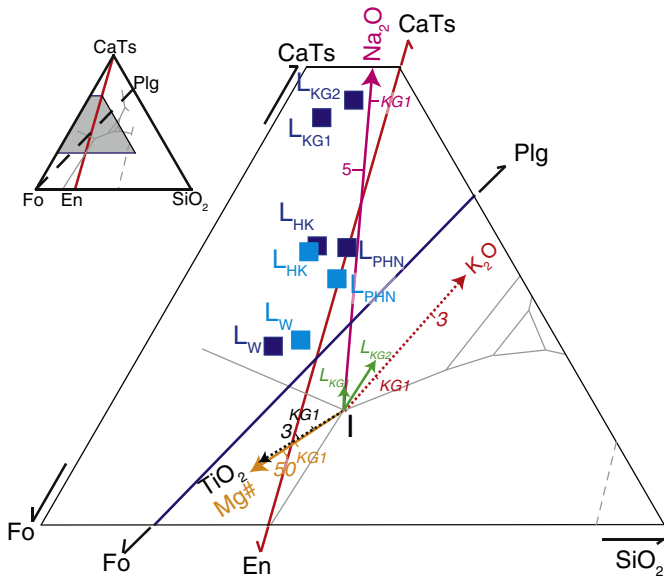


Fig. 4. Projection from Di on Fo–CaTs–Qz of melts in equilibrium with Ol, Opx, Cpx and Sp derived from KG1 (L_{KG1}), KG2 (L_{KG2}), W3 (L_W), HK66 (L_{HK}) and PHN1611 (L_{PHN}) at 2 GPa (dark blue squares; Hirose and Kushiro, 1993; Kogiso et al., 1998; Kushiro, 1996; Parman and Grove, 2004), using the O'Hara's method (1972). Light gray lines describe the diopside-saturated liquidus surface in the CMAS system projected from Di on the Fo–CaTs–Qz plane (see Fig. 3); point I corresponds to the melt in equilibrium with Ol, Opx, Cpx and Sp (an isobaric invariant point in the CMAS system). The pink and orange arrows represent the linear axes $[Na_2O]$ and $[Mg\#]$ inferred from data in the CMASN and CMASF systems (see Fig. 3). The displacement away from I is equal to $[-0.026Fo + 0.045CaTs - 0.019SiO_2] * Na_2O$ along $[Na_2O]$, where Na_2O is the melt content in mol%, and to $[0.036Fo - 0.082CaTs - 0.054SiO_2] * (1 - Mg\# / 100)$ along $[Mg\#]$, where $Mg\#$ is the molar ratio $100 * Mg^{2+} / [Mg^{2+} + Fe^{2+}]$. The green arrows represent the difference between the position of I and the position of L_{KG1} and L_{KG2} corrected from the Na_2O and $Mg\#$ effects. The red and black dashed arrows respectively represent the linear axes $[K_2O]$ and $[TiO_2]$ inferred from compositions of L_{KG1} and L_{KG2} assuming the effect of Cr_2O_3 as negligible (see text). The displacement away from I is equal to $[-0.039Fo + 0.039CaTs + 0.013SiO_2] * K_2O$ along $[K_2O]$, and to $[0.017Fo - 0.010CaTs - 0.007SiO_2] * TiO_2$ along $[TiO_2]$, with K_2O and TiO_2 , the melt contents in mol%. Graduations on axes are in molar percent on vectors $[TiO_2]$, $[K_2O]$ and $[Na_2O]$ and $Mg\#$ on the vector $[Mg\#]$ and quantify the effect of each oxide: e.g., the graduation "3" on $[TiO_2]$ represents the position of I in the system CMAS + TiO_2 when the TiO_2 content of melt equals 3 mol%. As an example, the individual contribution of each element to the position of liquid L_{KG1} is shown by the graduation labeled "KG1" on the four linear axes. Light blue squares represent the positions of L_W , L_{HK} and L_{PHN} calculated from vectors $[Na_2O]$, $[Mg\#]$, $[K_2O]$ and $[TiO_2]$.

Cr_2O_3 contents in L_{KG1} and L_{KG2} are very low (0.02 mol%; Table S2 in the supplementary material), thus, even with a potential effect of Cr_2O_3 on phase relations at high pressure (Liu and O'Neill, 2004a), it should remain negligible in the present case. Therefore, the residual vectors should mainly reflect the effects of K_2O and TiO_2 allowing us to draw the linear axes $[K_2O]$ and $[TiO_2]$ in Fig. 4, which indicate the displacement of point I as a function of the mol% of K_2O or TiO_2 into the melt. Results are consistent with previous studies: (1) the addition of K_2O produces a strong expansion of the Ol phase volume and, unlike Na_2O , tends to increase the degree of silica saturation of the melt (Liu and O'Neill, 2004b); and (2) TiO_2 has the opposite effect and tends to move liquidus boundaries between minerals toward the silica deficient side of systems (Mysen et al., 1980; Wood and Hess, 1980). Moreover, we underline that the effects of TiO_2 and $Mg\#$ are similar. Hence, while the effect of iron on the melting relations of peridotites does not seem to be significant (e.g., Gudfinnsson and Presnall, 2000), taking into account the large compositional range of pyroxenites ($TiO_2 \sim 0\text{--}5\%$, $Mg\# \sim 35\text{--}95$; Fig. 1), the effects of iron and titanium on phase relations are of the same magnitude.

In order to test the validity of the model, we considered other liquids in equilibrium with Ol, Opx, Cpx and Sp at 2 GPa. To our knowledge, only three more anhydrous melt compositions are reported in the literature, produced respectively by the peridotite HK66 at 1350 °C (L_{HK} ; Hirose and Kushiro, 1993), the peridotite PHN 1611 (L_{PHN} ; Kushiro, 1996) at 1350 °C and the basalt–peridotite mix W3 at 1425 °C (L_W ; Parman and Grove, 2004). Compositions of these melts are reported in Table S2 in the supplementary material. In Fig. 4, the theoretical positions of liquids L_{HK} , L_{PHN} and L_W computed using the four linear axes $[TiO_2]$, $[Na_2O]$, $[K_2O]$, and $[Mg\#]$ plot close to the experimental liquid. Thus, our linear model reproduces reasonably well the compositional effect on the phase relations. The differences may be due to several factors: (i) the analytical and experimental errors on melt compositions, (ii) the potential fluid content of liquids that could affect the phase relations, and (iii) the effect of additional minor oxides, such as P_2O_5 . For instance, compositions reported by Kogiso et al. (1998) are normalized to 100% and we cannot exclude small percentages of dissolved H_2O and CO_2 (due to the use of gel in starting compositions, a highly hygroscopic material, and of graphite capsule). Similarly, the P_2O_5 content in the case of L_W is relatively high (0.31 mol%; Table S2 in the supplementary material) and could lead to the shrinking of the Ol phase volume (Kushiro, 1975; Liu and O'Neill, 2007).

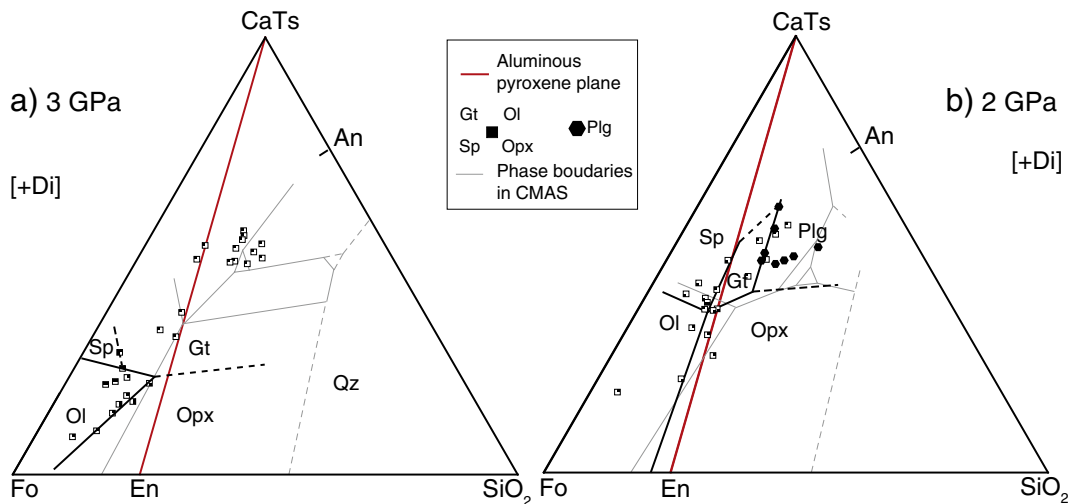


Fig. 5. Liquidus phase of natural compositions (bold black lines) (a) at 3 GPa and (b) at 2 GPa. Data includes both assemblages saturated with cpx and not saturated with cpx (see Table S1 for references). Diopside saturation surface in the CMAS, based on Milholland and Presnall's experimental data (1998) at 3 GPa and on Liu and Presnall's experimental data (2000) at 2 GPa, are given for comparison (fine gray lines). Abbreviations are as in Fig. 2. We used the O'Hara's method (1972) for the projection.

Table 1

Summary of run information: pressure, temperature, duration, phase proportions and compositions (wt.%) and composition of starting materials.

	Mode	SiO ₂	TiO ₂	Al ₂ O ₃	Cr ₂ O ₃	FeO	MnO	MgO	CaO	Na ₂ O	K ₂ O	Total	Mg# ^a	K _D ^b
<i>Run 40-L3 (2 GPa–1200 °C), 122 h</i>														
cpx (8)	54 (4)	52.1 (4)	0.44 (9)	7.0 (3)	0.14 (4)	6.6 (4)	0.14 (3)	15.5 (4)	15.6 (9)	2.49 (8)	0.00 (1)	99.7 (4)	80.6 (7)	
gt (9)	26 (7)	41.9 (2)	0.3 (1)	22.8 (3)	0.18 (6)	12.4 (3)	0.34 (5)	16.5 (6)	5.6 (8)	0.03 (7)	0.00 (2)	99.4 (5)	70.3 (8)	
plg (6)	5 (1)	63 (2)	0.6 (1)	24 (1)	0.00 (3)	3.2 (9)	0.05 (4)	0.6 (4)	3.2 (9)	3.9 (9)	0.9 (2)	98.5 (2)		
opx (6)	13 (4)	53.5 (7)	0.18 (5)	6 (1)	0.10 (3)	11.1 (3)	0.16 (4)	27.1 (6)	1.5 (2)	0.33 (5)	0.01 (1)	99.5 (5)	81.3 (6)	
sp (4)	1 (2)	0.2 (1)	0.20 (7)	64.8 (4)	0.7 (3)	18.3 (4)	0.13 (6)	15.5 (4)	0.15 (5)	0.00 (3)	–	98.4 (1)	60.2 (4)	
<i>Run 40-J3 (2 GPa–1250 °C), 121 h</i>														
liq (6)	1.1 (3)	53.1 (7)	1.3 (2)	18.6 (3)	0.01 (8)	7.3 (4)	0.09 (8)	4.2 (2)	4.2 (2)	6.5 (4)	4.8 (4)	97 (1)	50.8 (1)	
cpx (9)	74 (3)	51.9 (4)	0.55 (6)	8.7 (9)	0.12 (5)	7.7 (5)	0.17 (6)	15.5 (6)	13.5 (7)	2.0 (2)	0.01 (2)	99.9 (8)	78.3 (8)	0.29
gt (6)	24 (4)	41.3 (3)	0.35 (8)	23.1 (3)	0.16 (6)	12.7 (2)	0.34 (6)	16.9 (7)	5.1 (8)	0.02 (3)	0.01 (4)	101.0 (4)	70.4 (9)	0.43
<i>Run 40-H3 (2 GPa–1275 °C), 148h^c</i>														
liq _{top} (9)	2.3 (5)	50.4 (6)	1.7 (2)	17.1 (3)	0.01 (8)	10.0 (4)	0.1 (1)	6.1 (2)	5.8 (3)	6.5 (3)	2.5 (2)	97.9 (8)	52.1 (2)	
liq _{bottom} (4)	2.2 (6)	50.4 (6)	1.6 (2)	17.0 (4)	0.01 (8)	10.1 (4)	0.13 (8)	6.2 (2)	6.0 (3)	6.2 (3)	2.4 (2)	97.7 (9)	52 (1)	
cpx (8)	73 (2)	51.9 (5)	0.52 (7)	8.52 (6)	0.13 (4)	7.6 (6)	0.16 (6)	15.6 (7)	14 (1)	1.9 (2)	0.01 (1)	100.4 (5)	78.6 (9)	0.30
gt (7)	25 (1)	41.5 (3)	0.4 (1)	23.1 (3)	0.14 (5)	12.4 (2)	0.35 (9)	16.8 (3)	5.4 (5)	0.03 (3)	0.00 (2)	100.9 (6)	71 (1)	0.45
<i>Run 40-F3 (2 GPa–1300 °C), 123 h</i>														
liq (9)	3.6 (9)	49.1 (8)	1.7 (2)	16.3 (5)	0.01 (8)	11.5 (4)	0.18 (8)	7.5 (2)	7.1 (3)	5.0 (1)	1.6 (2)	98 (2)	53.6 (8)	
cpx (6)	74 (3)	51.5 (7)	0.49 (8)	9.1 (9)	0.14 (6)	7.6 (9)	0.16 (7)	16 (1)	14 (2)	1.8 (2)	0.01 (3)	100.1 (9)	78.6 (9)	0.31
gt (10)	22 (2)	41 (1)	0.4 (1)	23.3 (9)	0.18 (8)	12.2 (4)	0.33 (7)	16.9 (4)	5.5 (6)	0.03 (4)	0.01 (3)	100.9 (6)	71 (1)	0.47
<i>Run 40-G3 (2 GPa–1350 °C), 126 h</i>														
liq (11)	19 (4)	47.0 (6)	1.4 (2)	16.5 (4)	0.02 (8)	12.3 (4)	0.2 (1)	9.9 (3)	9.3 (3)	3.2 (2)	0.24 (6)	98 (1)	58.8 (8)	
cpx (16)	69(4)	50.9 (4)	0.31 (6)	9.9 (4)	0.17 (6)	7.1 (4)	0.20 (9)	17.3 (4)	12.9 (4)	1.2 (1)	0.01 (2)	99.8 (6)	81 (1)	0.33
gt (6)	12 (3)	41.8 (4)	0.4 (1)	23.3 (3)	0.17 (5)	10.4 (4)	0.33 (8)	18.01 (4)	5.6 (5)	0.01 (2)	0.01 (3)	100.5 (6)	76 (1)	0.46
<i>Run 40-C3 (2 GPa–1375 °C), 123 h</i>														
liq (4)	25 (2)	47.3 (6)	1.1 (1)	15.7 (3)	0.03 (8)	12.3 (4)	0.2 (1)	10.4 (3)	9.2 (5)	3.5 (3)	0.26 (7)	97 (2)	60.3 (8)	
cpx (8)	66 (3)	50.9 (5)	0.30 (8)	9.8 (7)	0.20 (6)	7.2 (3)	0.19 (6)	17.6 (5)	12.8 (4)	1.09 (8)	0.01 (2)	99.1 (7)	81.3 (6)	0.35
gt (8)	10 (3)	41.4 (2)	0.36 (4)	23.4 (4)	0.20 (7)	10.5 (4)	0.32 (3)	18.0 (2)	5.8 (4)	0.01 (2)	0.00 (1)	99.9 (3)	75.4 (9)	0.49
<i>Run 40-C3b (2 GPa–1375 °C), 126 h</i>														
liq (9)	27 (2)	47.3 (6)	1.1 (1)	15.6 (3)	0.03 (8)	12.2 (4)	0.23 (9)	10.6 (3)	9.6 (3)	3.1 (2)	0.23 (8)	98 (1)	60.9 (7)	
cpx (9)	66 (3)	50.7 (8)	0.30 (7)	10 (1)	0.17 (6)	7.1 (2)	0.18 (6)	17.5 (6)	12.8 (5)	1.1 (1)	0.01 (2)	99.9 (4)	81.4 (6)	0.35
gt (8)	7 (3)	41.2 (3)	0.5 (1)	23.2 (3)	0.16 (8)	10.3 (3)	0.36 (5)	18.2 (3)	6.1 (4)	0.02 (3)	0.01 (2)	100.6 (4)	73.0 (9)	0.49
<i>Run 40-E3 (2 GPa–1400 °C), 99 h</i>														
liq (8)	69 (3)	47.5 (6)	0.7 (1)	14.7 (4)	0.07 (9)	9.9 (4)	0.2 (2)	13.7 (3)	11.1 (4)	2.0 (2)	0.10 (8)	99 (1)	71.1 (8)	
cpx (8)	32 (3)	51.5 (5)	0.15 (5)	8 (1)	0.28 (7)	5.4 (2)	0.18 (6)	20.7 (9)	12.7 (5)	0.7 (1)	0.02 (4)	99.8 (8)	87.2 (6)	0.36
<i>Run 40-K3 (2 GPa–1450 °C), 97 h</i>														
liq	100													
<i>Run 40-E4 (2.5 GPa–1375 °C), 106 h</i>														
liq (9)	2.6 (3)	48.3 (7)	2.08 (9)	15.8 (5)	0.00 (8)	12 (1)	0.19 (5)	7.3 (2)	7.0 (3)	5.5 (2)	2.2 (2)	98.1 (9)	53 (3)	
cpx (8)	69 (2)	51.3 (4)	0.53 (9)	8.9 (4)	0.13 (6)	7.8 (5)	0.2 (1)	15.5 (6)	13.7 (9)	1.9 (2)	0.01 (2)	99.5 (7)	78.0 (9)	0.31
gt (9)	29 (2)	41.0 (4)	0.5 (1)	22.9 (2)	0.2 (2)	12.2 (4)	0.32 (6)	16.9 (8)	6.0 (1)	0.04 (4)	0.01 (1)	100.6 (6)	71 (1)	0.44
<i>Run P40-25 (2.5 GPa–1400 °C), 115h^d</i>														
liq (10)	4.5 (6)	48.7 (6)	1.9 (2)	14.6 (3)	0.01 (8)	12.2 (4)	0.19 (8)	8.4 (2)	8.4 (3)	4.2 (3)	1.4 (2)	98.7 (6)	55 (1)	
cpx (8)	72 (2)	51.4 (4)	0.45 (6)	8.8 (7)	0.14 (7)	7.7 (4)	0.19 (6)	16.0 (9)	13.4 (6)	1.8 (2)	0.00 (0)	99.3 (6)	79 (1)	0.33
gt (6)	24 (2)	41 (1)	0.4 (1)	23 (1)	0.2 (2)	11.6 (3)	0.32 (5)	17.2 (7)	5.9 (8)	0.1 (2)	0.01 (3)	100.5 (5)	73 (1)	0.46
<i>Run 40-D4 (2.5 GPa–1425 °C), 112 h</i>														
liq (7)	14 (3)	47.2 (6)	1.7 (2)	15.3 (6)	0.02 (8)	11.9 (6)	0.17 (8)	10.3 (5)	9.8 (5)	3.2 (2)	0.40 (9)	98 (1)	61 (2)	
cpx (6)	69 (3)	51 (1)	0.4 (1)	10 (3)	0.2 (1)	7.1 (3)	0.21 (6)	16.7 (3)	13.4 (5)	1.5 (7)	0.01 (2)	99.6 (4)	81 (2)	0.37
gt (5)	16 (2)	41.3 (3)	0.40 (7)	23.2 (3)	0.21 (3)	10.7 (2)	0.3 (1)	18.3 (1)	5.6 (2)	0.02 (4)	0.01 (2)	100.9 (3)	75.3 (4)	0.51
<i>Run 40-D4b (2.5 GPa–1425 °C), 92 h</i>														
liq (7)	20 (3)	47.9 (8)	1.4 (3)	15.1 (3)	0.03 (8)	11.3 (4)	0.25 (9)	10.8 (3)	9.9 (4)	3.1 (2)	0.34 (9)	97.2(1)	63 (8)	
cpx (6)	57 (4)	51.0 (9)	0.36 (8)	9.5 (3)	0.16 (9)	7.1 (3)	0.22 (6)	16.7 (9)	13.4 (4)	1.48 (7)	0.01 (2)	99.8 (4)	81 (3)	0.37
gt (5)	23 (4)	41.4 (2)	0.42 (7)	23.2 (3)	0.19 (2)	10.6 (1)	0.32 (8)	18.26 (9)	5.6 (2)	0.02 (4)	0.01 (2)	100.9 (3)	75.4 (4)	0.51
<i>Run 40-F4 (2.5 GPa–1450 °C), 97 h</i>														
liq (9)	76 (5)	47.7 (6)	0.6 (1)	13.8 (5)	0.11 (9)	9.3 (3)	0.23 (8)	14.6 (3)	11.9 (4)	1.7 (2)	0.07 (6)	98 (1)	73.7 (4)	
cpx (9)	25 (5)	52.2 (1)	0.13 (5)	8.2 (2)	0.3 (1)	5 (1)	0.20 (6)	21 (2)	12 (1)	0.8 (1)	0.00 (2)	100.2 (7)	89 (3)	0.37
<i>Run 40-B4 (2.5 GPa–1475 °C), 102 h</i>														
liq	100													
<i>Run 16-E3 (2 GPa–1250 °C), 121 h</i>														
cpx (8)	55 (2)	48.6 (4)	0.99 (9)	9.4 (5)	0.07 (4)	9.4 (2)	0.16 (6)	11.2 (3)	19.0 (3)	1.14 (8)	0.01 (2)	100.3 (5)	68.1 (5)	
gt (9)	38 (2)	39.9 (7)	0.3 (4)	22.1 (3)	0.05 (7)	19 (2)	0.5 (1)	11.3 (7)	7 (2)	0.01 (3)	0.01 (2)	101.1 (6)	51 (2)	
ol (4)	7 (1)	36.7 (4)	0.05 (6)	0.15 (8)	0.02 (5)	33.8 (5)	0.39 (9)	29 (1)	0.7 (3)	–	–	99.4 (7)	60.1 (3)	

Table 1 (continued)

	Mode	SiO ₂	TiO ₂	Al ₂ O ₃	Cr ₂ O ₃	FeO	MnO	MgO	CaO	Na ₂ O	K ₂ O	Total	Mg# ^a	K _D ^b
<i>Run 16-B3 (2 GPa–1300 °C), 120 h</i>														
	liq (2)	7 (1)	38.2 (5)	3.3 (2)	10.7 (3)	0.02 (8)	25.0 (5)	0.39 (8)	8.8 (3)	10.7 (5)	2.5 (4)	0.48 (9)	94 (1)	38.6 (1)
	cpx (10)	60 (2)	48.4 (5)	0.7 (1)	9.4 (8)	0.06 (8)	9.9 (2)	0.22 (8)	12.3 (4)	18.1 (4)	0.9 (1)	0.01 (2)	99.7 (6)	69 (1) 0.28
	gt (7)	27 (2)	39.7 (4)	0.4 (3)	22.5 (1)	0.07 (4)	18 (3)	0.5 (1)	11.8 (9)	7 (2)	0.01 (2)	0.01 (2)	100.7 (5)	54 (3) 0.54
	ol (7)	3.3 (5)	37.4 (4)	0.06 (3)	0.4 (2)	0.00 (7)	28.4 (5)	0.38 (6)	33.4 (6)	0.8 (2)	–	–	99.1 (3)	67.7 (8) 0.30
	sp (3)	2.2 (7)	0.8 (5)	0.8 (2)	58 (1)	1 (1)	25.0 (5)	0.18 (6)	13.9 (2)	0.5 (5)	0.00 (0)	–	98.9 (7)	49.8 (7) 0.63
<i>Run 16-A3 (2 GPa–1300 °C), 118 h</i>														
	liq (17)	16 (3)	40.4 (5)	1.7 (2)	12.7 (3)	0.03 (8)	23.4 (5)	0.35 (1)	8.8 (2)	11.0 (4)	1.6 (2)	0.13 (6)	98 (1)	40.0 (5)
	cpx (10)	66 (2)	48.2 (4)	0.49 (7)	9.8 (4)	0.07 (3)	9.6 (4)	0.3 (8)	13.1 (2)	17.8 (4)	0.66 (7)	0.01 (3)	100.0 (7)	70.9 (7) 0.28
	gt (6)	12 (4)	39.8 (4)	0.50 (5)	22.7 (3)	0.07 (3)	16.2 (4)	0.6 (1)	12.5 (5)	7.7 (3)	0.02 (1)	0.01 (2)	100.7 (5)	58 (1) 0.49
	ol (5)	1.6 (7)	37.5 (5)	0.03 (6)	0.17 (5)	0.00 (4)	28.9 (6)	0.4 (1)	32.5 (9)	0.6 (2)	–	–	100.0(6)	67 (1) 0.33
	sp (5)	4 (1)	0.32 (5)	0.34 (6)	61.4 (6)	0.9 (1)	21.7 (2)	0.17 (7)	15.0 (3)	0.20 (6)	0.00 (3)	–	99.7 (7)	55.1 (3) 0.54
<i>Run 16-F3 (2 GPa–1325 °C), 114 h</i>														
	liq (19)	33 (1)	41.4 (5)	1.4 (2)	13.2 (3)	0.01 (8)	21.7 (5)	0.4 (1)	9.6 (3)	11.1 (4)	1.2 (1)	0.07 (7)	99 (1)	46 (1)
	cpx (9)	60 (1)	48.7 (5)	0.40 (6)	9.9 (4)	0.07 (4)	9.3 (3)	0.25 (6)	14.1 (3)	16.8 (3)	0.53 (6)	0.00 (1)	100.4 (6)	73.0 (8) 0.29
	gt (3)	3 (2)	40.3 (5)	0.4 (1)	22.9 (2)	0.07 (4)	15.2 (6)	0.54 (3)	13.4 (7)	7.2 (4)	0.00 (0)	0.00 (0)	101 (2)	61 (2) 0.50
	sp (7)	4.7 (5)	0.37 (5)	0.22 (6)	63.1 (3)	0.87 (9)	18.6 (3)	0.2 (1)	16.4 (3)	0.23 (9)	0.03 (5)	–	100 (1)	61.0 (6) 0.50
<i>Run 16-C3 (2 GPa–1350 °C), 125 h</i>														
	liq (10)	50.7 (5)	42.6 (5)	1.2 (2)	13.6 (3)	0.02 (8)	18.5 (6)	0.4 (1)	10.6 (3)	12.0 (4)	1.1 (1)	0.06 (4)	98.5 (5)	51 (1)
	cpx (18)	40.7 (5)	48.5 (4)	0.37 (6)	10.1 (4)	0.06 (5)	8.5 (6)	0.25 (6)	14.6 (3)	17.1 (3)	0.47 (6)	0.00 (1)	100 (1)	76 (1) 0.33
	sp (8)	3.6 (1)	0.38 (5)	0.20 (5)	63.7 (3)	0.9 (4)	16.6 (4)	0.18 (6)	17.9 (3)	0.21 (5)	0.00 (2)	–	99.1 (5)	65.7 (7) 0.53
<i>Run 16-G3 (2 GPa–1400 °C), 96 h</i>														
	liq	100												
<i>Run 16-D4 (2.5 GPa–1325 °C), 120 h</i>														
	cpx (6)	55 (2)	48.4 (8)	0.9 (1)	10 (1)	0.07 (5)	8.8 (5)	0.15 (1)	11.2 (2)	19.5 (7)	1.2 (9)	0.02 (4)	100.5 (3)	70 (1)
	gt (6)	37 (2)	39.9 (2)	0.4 (4)	22.2 (2)	0.06 (5)	18 (3)	0.50 (5)	11.2 (1)	8 (2)	0.02 (5)	0.00 (1)	100.8 (7)	53 (2)
	ol (3)	7.5 (8)	36.5 (4)	0.07 (5)	0.3 (3)	0.01 (5)	33.8 (5)	0.40 (7)	28.6 (2)	0.64 (6)	–	–	99.4 (7)	60.1 (3)
<i>Run 16-B4 (2.5 GPa–1350 °C), 107 h</i>														
	liq (3)	8 (1)	36.7 (5)	2.7 (3)	9.3 (2)	0.00 (8)	25.5 (9)	0.35 (8)	9.9 (3)	12.6 (5)	2.7 (3)	0.25 (7)	95.0 (9)	41 (2)
	cpx (8)	53 (2)	48.8 (4)	0.67 (7)	9.3 (4)	0.07 (3)	9.3 (4)	0.16 (8)	12.0 (2)	18.7 (4)	1.02 (7)	0.01 (3)	99.8 (9)	70 (1) 0.30
	gt (6)	36.5 (9)	39.9 (4)	0.3 (4)	22.3 (3)	0.1 (1)	18 (1)	0.49 (5)	12.4 (4)	7 (1)	0.01 (2)	0.01 (2)	100.7 (4)	55 (2) 0.56
	ol (6)	2.5 (5)	37.4 (5)	0.05 (3)	0.18 (5)	0.02 (5)	27.2 (4)	0.33 (7)	34.2 (5)	0.6 (1)	–	–	100.0 (8)	69.2 (5) 0.31
<i>Run P16-25 (2.5 GPa–1400 °C), 98 h^d</i>														
	liq (12)	22 (2)	39.1 (5)	2.4 (2)	10.4 (3)	0.01 (8)	22.2 (5)	0.4 (1)	10.6 (4)	12.8 (4)	1.9 (2)	0.18 (8)	98.1 (8)	46 (1)
	cpx (8)	46 (2)	48.7 (6)	0.54 (6)	9.8 (8)	0.09 (3)	8.3 (3)	0.16 (6)	12.7 (4)	18.8 (4)	0.90 (9)	0.00 (1)	100.2 (8)	73 (1) 0.31
	gt (5)	32 (2)	40.3 (4)	0.4 (3)	22.8 (3)	0.07 (3)	14.8 (2)	0.45 (5)	13.1 (9)	8 (2)	0.01 (2)	0.01 (3)	100.9 (7)	61 (2) 0.54
<i>Run 16-C4b (2.5 GPa–1425 °C), 101 h</i>														
	liq (3)	65 (2)	42.3 (7)	1.0 (2)	14.3 (4)	0.05 (9)	16.9 (4)	0.3 (2)	10.9 (3)	13.2 (6)	1.1 (2)	0.06 (7)	96.4 (8)	54 (1)
	cpx (7)	25 (2)	48.4 (5)	0.48 (7)	10.5 (4)	0.09 (3)	7.1 (3)	0.19 (8)	14.0 (2)	18.5 (3)	0.81 (7)	0.01 (3)	99.6 (6)	78 (2) 0.33
	gt (6)	9 (2)	40.6 (4)	0.3 (3)	23 (3)	0.1 (1)	14 (2)	0.5 (1)	14.7 (9)	7 (2)	0.02 (2)	0.01 (2)	100.7 (8)	65 (2) 0.61
<i>Starting materials</i>														
	M5-40	48.53	0.52	12.37	0.12	9.02	0.2	16.64	10.89	1.65	0.06		76.7	
	M7-16	43.58	0.75	13.73	0.07	14.51	0.30	12.52	13.77	0.75	0.03		60.6	

All the experiments were performed in Laboratoire Magmas et Volcans, Clermont-Ferrand, except 40-L3, which was made at the California Institute of Technology; see the supplementary material for technical details. The first term of the run numbers, 40 or 16, refers to the bulk composition M5-40 and M7-16, respectively. Phase compositions were analyzed with the electron microprobe; the number of analyses is given in parentheses in the first column. All compositions are normalized to a sum of 100 wt.% (the analytical total before normalization is reported in the column Total). For a given phase in a given sample, we calculated the statistical dispersion of the dataset (as measured by 2σ , where σ is the standard deviation) and the analytical error (following [Ancy, et al., 1978](#)), and we selected the largest of these two values as an estimation of the error. The errors (in parentheses) are given in terms of the least unit cited. Modes (in wt.%) are calculated using a mass-balance program modified from [Albarède and Provost \(1977\)](#); the number in parentheses is 2σ , given in terms of the least unit cited.

^a Mg# is the molar ratio $100\text{Mg}^{2+}/(\text{Mg}^{2+} + \text{Fe}^{2+})$; we considered that all iron was as Fe^{2+} .

^b Fe–Mg exchange coefficients between mineral and melt: $[\text{K}_D] = (\text{Fe}/\text{Mg})^{\text{mineral}}/(\text{Fe}/\text{Mg})^{\text{melt}}$.

^c Compositions of glasses analyzed in microdikes at the bottom (liq_{bottom}) and at the top (liq_{top}) are given.

^d P40-25 and P16-25 are from [Lambart et al. \(2012\)](#).

To summarize the effect of non-CMAS elements on phase relations, we compare in [Fig. 5](#) the experimentally determined liquidus phase relations of natural pyroxenites and the liquidus phase relations in the CMAS system at 2 and 3 GPa. Even though it is difficult to delineate the role of each non-CMAS element, it is clear that the Gt phase volume is significantly larger in natural compositions and already crosses the aluminous pyroxene plane at 2 GPa. Moreover, the Ol–Opx boundary in natural pyroxenites is shifted toward Fo, reducing further the Ol

phase volume and increasing that of Opx. Finally, a third major difference between the CMAS system and natural pyroxenites is that the Sp volume is much smaller in the latter than in the former: in natural pyroxenites, the Sp volume is almost fully restricted to the left of the CaTs–En join, even at 2 GPa. Thus, for natural compositions, the thermal divide becomes effective at pressures lower than 2 GPa and, compared to the CMAS system, the range of compositions under its influence expands to include compositions richer in CaTs component.

2.2. Melt composition variability

In this section, based on previous and new experimental data, we examine the effect of the garnet–pyroxene thermal divide on the relationship between bulk and melt compositions. First, we consider the case of pressures ≥ 2 GPa, and we pay special attention to the effect of the thermal divide at low melt fractions (low- F), an issue that has hardly been discussed in the literature. Then, we look at the relationship between bulk and melt compositions at lower pressure, at which the thermal divide is not effective anymore. Finally, we discuss the effects of the presence of fluids (H_2O , CO_2).

2.2.1. Melts compositions and thermal divide

At pressures ≥ 2 GPa, the garnet–pyroxene divide is effective; melts derived from a given bulk composition are on the same side of the divide than their parent rock and the evolution of these melts by partial melting and/or crystallization is also confined to this side. Based on phase relations in the CMAS system and on melts produced at moderate to high degrees of melting of natural pyroxenites, it was suggested that the thermal divide leads to strongly contrasting melt compositions, especially in SiO_2 content; that is, it would lead to strongly contrasting trends in silica for compositions on the opposite sides of the plane. Kogiso et al. (2004a) proposed a “barrier” close to 48 wt.% SiO_2 in melts: SD pyroxenites would produce melts with less than 48 wt.% SiO_2 , and SE pyroxenites would produce melts with more than 48 wt.% SiO_2 . Herzberg (2006, 2011) also placed this barrier close to 48 wt.% for primary pyroxenite magmas from Hawaii. His estimation was obtained by plotting the compositions of Hawaiian basalts after correction for Ol fractionation in the CaTs–Di–Qz–Ol system: liquids nearest to the pyroxene–garnet plane contained ~ 48.2 wt.% SiO_2 . However, very few data exist on melt compositions derived from pyroxenites at low- F (Lambart et al., 2009; Pertermann and Hirschmann, 2003; Spandler et al., 2008). Moreover, at pressures at which the thermal divide is effective (≥ 2 GPa), almost no data are available on SD pyroxenites at low melting degrees.

Lambart et al. (2012) described an experiment performed at 2.5 GPa and 4.5 wt.% of melting on the slightly silica-deficient pyroxenite M5-40 (Tables 1, S1 in the supplementary material). Except this experiment, no melt composition is, to our knowledge, reported at melting degrees lower than 15%. Yet low- F liquids are enriched in elements (TiO_2 , Na_2O , K_2O , and in cases, FeO ; Lambart et al., 2009, 2012) that can strongly influence the phase relations and thus the silica content of melt. Therefore we performed new experiments in a piston–cylinder apparatus at 2 and 2.5 GPa using M5-40 and the more silica-deficient pyroxenite M7-16 (Figs. 1, 2; Table 1) as starting materials. M5-40 is a garnet (Gt) websterite, close to the mean composition of the natural pyroxenite population. M7-16 has a more extreme composition, with low SiO_2 and high FeO contents. The criteria used to select these two samples were discussed in Lambart et al. (2009). Compositions and proportions of phases are given in Table 1. Experimental and analytical techniques are reported in the supplementary material (Appendix 1 and Figs. S1–S4 in the supplementary material). Using the microdike technique developed by Laporte et al. (2004), we have determined the melt compositions at melting degrees as low as 1.2 wt.% (Fig. 6). These new experiments significantly increase the amount of available data on the compositions of low- F liquids of pyroxenites at high pressures.

Fig. 7 presents the evolution of melt compositions derived from pyroxenites at pressures between 2 and 5 GPa projected from Di on the plane Fo–CaTs–Qz (Fig. 7a) and from CaTs on the plane Fo–Di–Qz (Fig. 7b). For a given composition, the effect of pressure on phase relations is small because the phase assemblages remain similar and mainly composed of Cpx and Gt. Experimental results suggest that the thermal divide is effective at this range of pressures, in agreement with the liquidus phase relations of natural compositions (Fig. 5): liquids from SD pyroxenites are far on the left of the aluminous pyroxene plane at low F , and approach this plane with increasing F ; liquids from SE

pyroxenites are far on the right at low F , and approach the aluminous pyroxene plane with increasing F . In detail, the compositional trends differ both between the two sides of the thermal divide and within one side (Fig. 7). On the silica-deficient side, first melts derived from M5-40 are strongly enriched in CaTs component (Fig. 7a). The enrichment of low- F melts in CaTs decreases from M5-40 to MIX1G, 77SL-582 and to M7-16. Low- F melts from M7-16 appear also extremely depleted in Qz component. Finally, the behavior of the Di component at high F seems to depend on the liquidus phase (Fig. S5b in the supplementary material). When Cpx is the liquidus phase (like in experiments on M5-40, M7-16 and MIX1G at 2 GPa), the Di component increases at high F while it decreases on the overall of the melting assemblage when the liquidus phase is not Cpx (like in experiments on 77SL-582, B-ECL1-OL and MIX1G at 5 GPa). On the silica-excess side, two types of SE pyroxenites can be distinguished (Herzberg, 2006): (1) compositions directly representing the recycled oceanic crust (basalt or gabbro), referred to as stage 1 SE pyroxenites in the following (G2, GA1, GA2, Gb 108 and CRB72-31), and (2) SE pyroxenites produced by the reaction of recycled material (or the corresponding derived melts) with surrounding peridotite, referred to as stage 2 SE pyroxenites in the following (Px-1). Unfortunately, most of high-pressure partial melting experiments on SE pyroxenites have been performed on stage 1 SE pyroxenites. Hence, the range of SE pyroxenites compositions experimentally investigated is very small and the behaviors reported for stage 1 SE pyroxenites mainly differ at low F . First melts of G2 are enriched in CaTs component and depleted in Di component (Fig. 7). On the contrary, the other stage 1 SE pyroxenites (Gb108, GA1, GA2, CRB72-31) tend to generate incipient melts more enriched in Qz component. Melts from the stage 2 SE pyroxenite Px-1 show a similar behavior than that of melts from CRB72-31 but are shifted towards compositions poorer in CaTs and Di components (Fig. 7a).

Fig. 8 presents the pyroxenite melt compositions as a function of F . For most elements, melt compositions from SD and SE pyroxenites largely overlap if the whole melting range is considered. In all compositions, the CaO content of liquid increases with F until Cpx disappearance (when it occurs). The range of CaO concentrations varies from 4.4 to 14.2 wt.% for SD pyroxenites and from 2.8 to 11.7 wt.% for SE pyroxenites, showing a large overlap between the two classes. Melts derived from SD and stage 1 SE pyroxenites present contrasted MgO contents: from 4.3 to 16.6 wt.% for melts from SD pyroxenites and from 1.2 to 8.1 wt.% for melts from SE pyroxenites. This directly reflects the difference of bulk compositions. However, in both categories, MgO increases progressively with F . Moreover, melts from the stage 2 SE pyroxenite Px-1 present a range of MgO contents (4.4–18.5 wt.%) that entirely overlaps the range of melts from SD pyroxenites. According to Herzberg (2006), stage 2 pyroxenites may cover a wide range of compositions depending on the melting degree undergone by the oceanic crust, and so include types intermediate between the stage 1 SE pyroxenites and composition Px-1.

Al_2O_3 shows various behaviors within both classes. With increasing F , Al_2O_3 decreases in melts from M5-40 and Px-1, and increases in melts from most other pyroxenites. Concentration ranges also show a wide overlap (6.4–18.4 wt.% for SD pyroxenite melts and 13.1–17.5 wt.% for SE pyroxenite melts). The lowest Al_2O_3 contents are observed in melts from MIX1G at 5 GPa due to the increased stability of Gt at this pressure. More importantly, SiO_2 displays a relatively incompatible behavior in SE pyroxenites and a predominantly neutral behavior (i.e., the content of the liquid does not change significantly) in SD pyroxenites, except at very low degrees of melting. This observation contrasts with the previous suggestion (Herzberg, 2006; Kogiso et al., 2004a; Schiano et al., 2000) that the silica content in melts from SD pyroxenites increases with F . Our results on M5-40 show that (1) the silica content of SD pyroxenite melts can decrease with F , and (2) this content can reach more than 52 wt.% at low- F (Fig. 8, Table 1).

We observe that, except for M7-16, the variation of FeO concentration in liquids is limited. On the contrary, in M7-16-derived melts, FeO

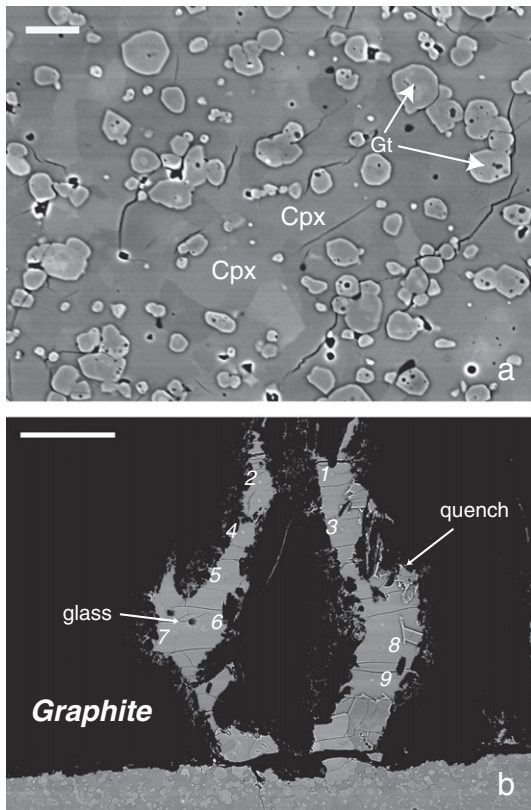


Fig. 6. (a) Backscattered electron image showing the phase assemblage of the partially molten pyroxenite M5-40 at 2 GPa and 1275 °C (#40-H3). The phase assemblage is Cpx + Gt + Liq; the interstitial melt is not perceptible owing to the very low melt fraction (2.3%) and growth of quench Cpx at the end of the experiment. (b) Backscattered electron image showing two microdikes in the graphite container of sample 40-H3: the graphite container is black and the partially molten pyroxenite is gray; the basaltic microdike contains large pools of glass and large crystals. Numbers show the positions of the melt analyses (see supplementary material, Fig. S2).

behaves as an incompatible element and decreases strongly with increasing F . These different behaviors of iron were previously documented at 1 and 1.5 GPa by Lambart et al. (2009), who suggested that the variation of the FeO content in pyroxenite melts is correlated with the bulk FeO content. K_2O is very incompatible; thus, at a given F , the K_2O content of melts depends on the initial content of the rock, but trends are broadly the same in all compositions. TiO_2 is also incompatible, except when rutile is present in the phase assemblage (i.e., near the solidus of G2 at 3 GPa and of GA2, Fig. 8). Finally, between 2 and 3 GPa, the behavior of Na_2O is controlled by the presence of feldspar in the assemblage. The Na_2O content of liquid increases until the disappearance of feldspar, then Na_2O behaves as an incompatible element. Moreover, at $P > 3$ GPa, the Na_2O content in melts does not change significantly due to the increase of the relative compatibility of Na_2O in residual Cpx (e.g., Pertermann and Hirschmann, 2003; Spandler et al., 2008).

Comparison of Fig. 8 with Figs. 4 and 7 allows us to better understand the relationship between melt composition and liquidus phase relations. Overall, low degree melts from SD pyroxenites range from highly enriched in iron for M7-16 to highly enriched in alkalis for M5-40; melts from MIX1G and 77-SL-582 are intermediate. These observations are fully consistent with the trends observed in the Fo–CaTs–Qz–Di system (Figs. 4, 7). Indeed, the alkali enrichment of melts produces a strong expansion of the Ol phase volume while the iron enrichment results in a contraction of this one in favor of more polymerized phases (Gt, Opx, Sp). Moreover, the addition of K_2O tends to increase the silica content of the melt. At 2 GPa, low

degree melts from M5-40 are very rich in K_2O (up to 4.8 wt.%, Table 1) and consequently, this enrichment is accompanied by silica enrichment. In the case of SE pyroxenites, melts from GA1 and GA2 are enriched in K_2O , melts from G2 are enriched in TiO_2 , and melts from Px-1 have intermediate contents. The first melts from G2 are depleted in SiO_2 in comparison to those of GA1 and GA2 (<55 wt.% vs. 60–65 wt.%, respectively; Fig. 8), but still they are saturated in quartz (Fig. S5 in the supplementary material). Accordingly, TiO_2 enrichment and K_2O depletion seem to induce a larger phase volume of Qz, as anticipated by Kushiro (1975).

To conclude, the garnet–pyroxene thermal divide indeed controls the melting relations of pyroxenites at high pressure (> 2 GPa) and SD and SE pyroxenites produce liquids with different compositions. Partial melts from SD pyroxenites generally have lower SiO_2 , and higher CaO and FeO contents than those from SE pyroxenites. For the other oxides, however, the differences in melt compositions from one pyroxenite to the other are mainly related to the difference of bulk compositions rather than to the presence of the thermal divide. As a rule, there is a progressive transition from the liquids derived from the most silica-deficient compositions to those derived from the most silica-excess compositions, rather than a sharp divide.

2.2.2. Melts compositions at pressures < 2 GPa

The disappearance of the thermal divide and the change of mineral assemblages at $P < 2$ GPa are likely to have a significant impact on the melting relations of pyroxenites. Indeed, while the phase assemblages are mainly composed of Cpx and Gt at $P = 2$ GPa, Gt becomes an accessory phase at $P < 2$ GPa, and the roles of Opx, Ol and/or Plg increase (Fig. 9; Kogiso et al., 2004a).

Lambart et al. (2009) studied the melting relations of three SD pyroxenites at 1 and 1.5 GPa: M5-40, M7-16 (Table 1), and M5-103, a more SiO_2 - and MgO-rich pyroxenite, close to an orthopyroxenite (Table S1 in the supplementary material). Most partial melts from M5-40 and M5-103 plot on the right side of the aluminous pyroxene plane (Fig. S6 in the supplementary material) attesting to the absence of a thermal divide at $P < 2$ GPa. Contrasted melting behaviors were observed depending on the presence of Opx and/or Plg at the solidus. If Opx is abundant, the main melting reaction is similar to the melting reaction in peridotites, that is $Cpx + Opx = Liq + Ol$. Accordingly, the chemical trends of melts from websterites mimic those of peridotitic melts despite major differences in the modal fractions of solid phases and in bulk compositions (Fig. 9). For the Opx-free pyroxenite M7-16, the main melting reaction (after Plg exhaustion) is $Cpx + Sp = Liq + Ol$, and liquids are strongly depleted in SiO_2 in comparison to liquids produced by Opx-bearing rock types. Finally, when Plg is present, the liquid does not undergo significant compositional changes. Thus, the melting behavior of pyroxenites at $P < 2$ GPa is no longer controlled by the aluminous pyroxene plane and melt compositions mainly depend on the abundance of Opx and/or Plg at the solidus. Lambart et al. (2009) showed that pyroxenite-derived liquids produced at $P < 2$ GPa have compositions similar to peridotite-derived liquids for most oxides (Fig. 9). A notable exception is the very silica-deficient pyroxenite M7-16, whose liquids are strongly depleted in SiO_2 in comparison to peridotite-derived melts.

2.2.3. The effect of fluids

Due to the potential role of H_2O and CO_2 in the source of basalts (e.g., Asimow and Langmuir, 2003; Bonatti, 1990), it is important to understand their role on melting relations and on liquid compositions. These two volatile components are present at low concentration levels in oceanic magmas source-regions (Michael, 1988; Saal et al., 2002), so their effects on liquidus phase relations are likely negligible. They could, however, have a significant impact on melt composition, and especially on the composition of the first-formed liquids due to their very incompatible behavior with respect to most mantle mineral phases. Compared to the fluid-absent case, we can expect that incipient melts of

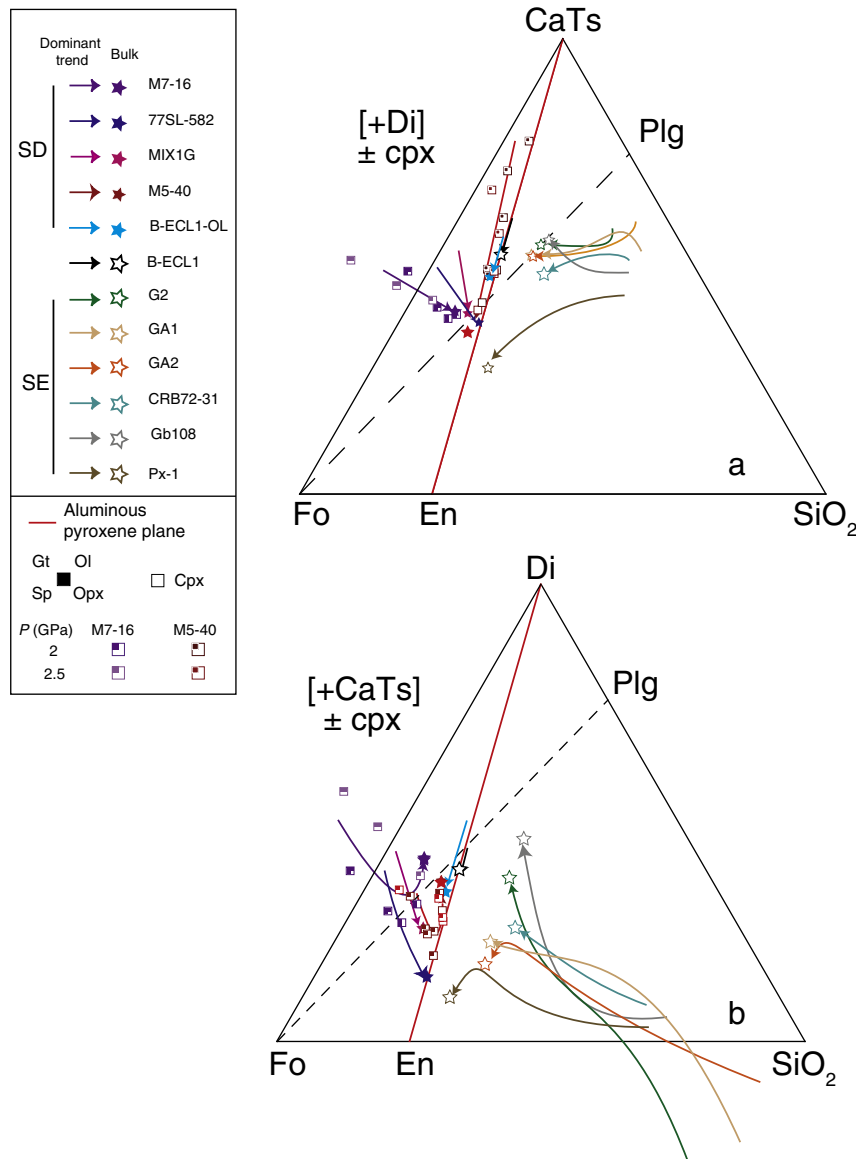


Fig. 7. Schematic representations of the evolution of melt composition with increasing melt fraction for each bulk pyroxenite composition between 2 and 5 GPa: the projection is from Di on the plane Fo–CaTs–Qz in (a) and from CaTs on the plane Fo–Di–Qz in (b). Phase assemblages and melt compositions in partial melting experiments of M5-40 and M7-16 at 2 and 2.5 GPa are also reported. See Fig. S5a–b in the supplementary material for more details. References are: M7-16 and M5-40, this study and Lambart et al. (2012); MIX1G, Hirschmann et al. (2003) and Kogiso et al. (2003); 77SL-582, Keshav et al. (2004); B-ECL1 and B-ECL1-OL, Kogiso and Hirschmann (2006); G2, Pertermann and Hirschmann (2003); GA1, Yaxley and Green (1998); GA2, Spandler et al. (2008); CRB72-31, Takahashi et al. (1998); Gb108, Yaxley and Sobolev (2007); and Px-1, Sobolev et al. (2007). Abbreviations and phase symbols are as in Fig. 3.

pyroxenites will be enriched in SiO₂ in the presence of H₂O, and depleted in SiO₂ in the presence of CO₂. The effect of H₂O is confirmed by experimental studies at high pressures on simple systems (Kushiro, 1972) and natural compositions (e.g., Green, 1973; Irving and Green, 2008; Nicholls and Ringwood, 1973), which show an important silica enrichment of melt for a given phase assemblage, along with a significant increase of the Ol phase volume in the presence of water. In the same way, Gaetani and Grove (1998) showed that hydrous peridotite melts are SiO₂-rich when compared to anhydrous melts on a volatile-free basis. In contrast, the presence of CO₂ significantly decreases the SiO₂ content of melts (Hirose, 1997). In the system peridotite + CO₂ at 3 GPa, Dasgupta et al. (2007) showed that the silica content of melts in equilibrium with Ol + Opx + Cpx + Gt decreases from 43.8 wt.% to 28.4 wt.% while the CO₂ content in melt increases from 13 to 25 wt.%. Near-solidus partial melting of carbonate-bearing mantle rocks (carbonated peridotites and pyroxenites) produces carbonatite melts (Dasgupta and Hirschmann, 2010; Yaxley and Brey,

2004). In terms of phase equilibria, the effect of CO₂ is to increase the stability of Gt at the expense of Cpx and Ol (e.g., Dasgupta et al., 2007); accordingly, the garnet–pyroxene thermal divide is expected to become effective at a lower pressure in the presence of CO₂ than in a fluid-absent system. Water has the opposite effect on the thermal divide because it increases the Ol phase volume.

3. Pyroxenites in oceanic basalt genesis

Several lines of evidence indicate that Ol-poor rock types such as pyroxenites may play an important role in basalt generation. This evidence includes the ubiquity these lithologies in the upper mantle, the various origins proposed for these rocks (e.g., Downes, 2007), and the fact that as the plutonic or metamorphic equivalents of basaltic magmas, they are readily envisioned as a component at depth that can be introduced into other sources as a heterogeneity (e.g., Schiano et al., 2000). Pyroxenites are therefore often invoked to explain variations in abundance of

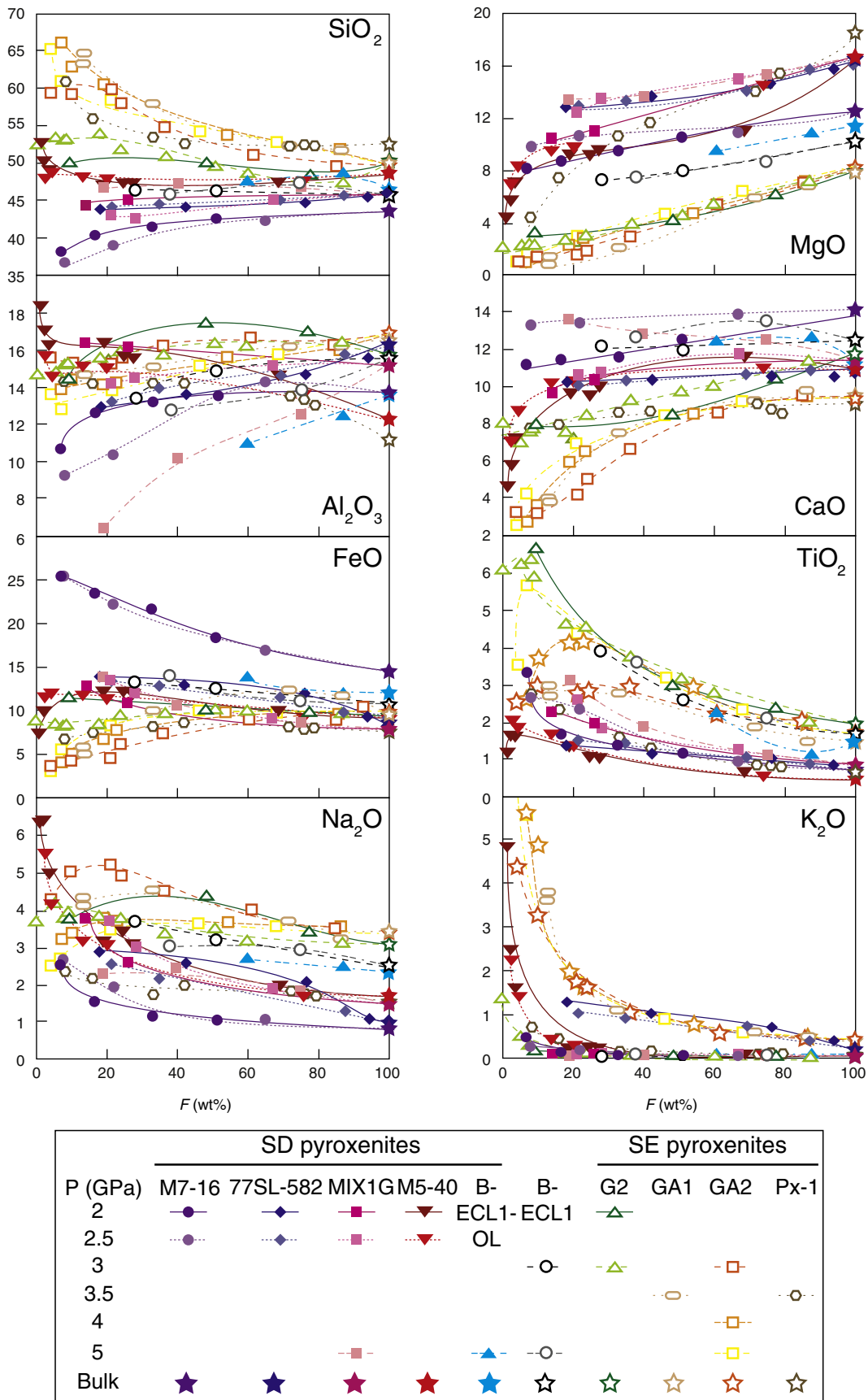


Fig. 8. Oxide content of liquids from partial melting experiments on pyroxenites between 2 and 5 GPa plotted as a function of melt fraction F . Symbols for each composition are given in the inset; same references and same colors as in Fig. 7.

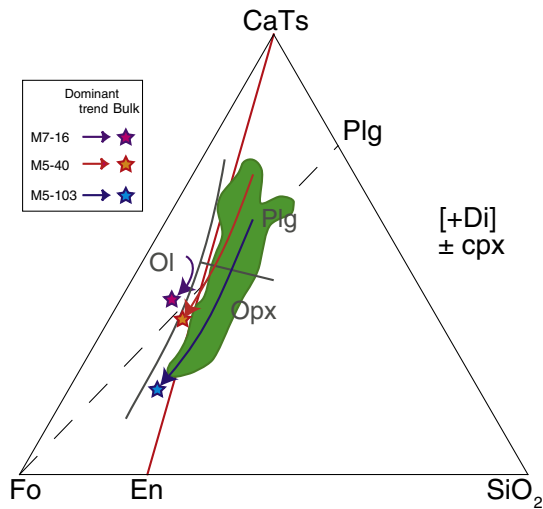


Fig. 9. Schematic representations of the evolution of melt composition with increasing melt fraction for pyroxenite compositions M7-16, M5-40 and M5-103 at 1–1.5 GPa (Lambart et al., 2009): the projection is from Di on the plane Fo–CaTs–Qz. A more detailed version of this figure is given in the supplementary material (Fig. S6). The green field corresponds to liquids produced by peridotites over the same pressure range (Baker and Stolper, 1994; Falloon and Danyushevsky, 2000; Hirose and Kushiro, 1993; Kushiro, 1996; Laporte et al., 2004; Robinson et al., 1998; Wasylenki et al., 2003). The gray lines are the liquidus phase boundaries at 1.5 GPa estimated by Kogiso et al. (2004a). Abbreviations as in Fig. 3.

trace elements and in isotope ratios both in OIBs and in MORBs (Allègre et al., 1995; Blichert-Toft et al., 1999; Hofmann, 1997; Sobolev et al., 2007). Therefore, some experimental studies were conducted to identify the fingerprints of the involvement of pyroxenite in the major-element composition of basalts. Our goal here is to determine the reliability of these markers and to discuss if they can help to quantify the proportions of pyroxenites in mantle source regions.

3.1. Pyroxenites in MORB source-regions

3.1.1. SiO_2 and FeO: barometers and/or markers of the pyroxenite contribution?

The impact of pyroxenites in source regions on the major-element compositions of MORB is still a matter of debate. Due to their high concentrations in pyroxenites (Fig. 1), alkali oxides and TiO_2 have been often considered as indicators of the heterogeneity of the mantle source (e.g., Le Roux et al., 2002; Niu et al., 1999, 2002). Lambart et al. (2009) showed, however, that, due to their lower solidus temperatures and higher degrees of melting compared to peridotites, pyroxenites yield partial melts that are not enriched in alkali oxides and TiO_2 in comparison to peridotite-derived melts in the physical conditions prevailing beneath mid-ocean ridges. Based on Icelandic basalt chemical trends, Shorttle and MacLennan (2011) recently suggested that pyroxenites could produce melts characterized by low SiO_2 and CaO, and high FeO. Although our results (Lambart et al., 2009) do not show CaO depletion in pyroxenite melts, they are consistent with the hypothesis that some pyroxenites can produce SiO_2 -poor and/or FeO-rich melts. The participation of such pyroxenite partial melts to MORB genesis could decrease the silica content and/or the Mg# of the aggregated melts erupted at mid-ocean ridges.

Based on partial melting experiments on peridotites, MORBs with MgO 9% and Mg# approaching 70 are often considered as the most primitive, and therefore the closest to primary liquids. In Melson and O'Hearn's (2003) database, 15% of the MORB glasses with MgO 9% have both a higher FeO content and a lower SiO_2 content than the usual primitive MORBs with Mg# 67 (Fig. 10, Table S3 in the supplementary material). According to Lambart et al. (2009), these compositions may be good candidates to represent primitive MORBs

carrying the signature of a silica-deficient pyroxenite. In this paper we term these particular compositions px-MORBs to emphasize the potential contribution of pyroxenite partial melts in their genesis.

Alternatively, lower SiO_2 and higher FeO contents could also reflect an increase of the average depth of melting due to higher mantle potential temperature (Klein and Langmuir, 1987; Langmuir et al., 1992) or to the fractionation of Cpx (e.g., Eason and Sinton, 2006). Fig. 11 shows the fractionation trends obtained with MELTS (Ghiorso and Sack, 1995) from a Model Primary Magma (MPM) as a function of pressure. The MPM composition has been calculated with PRIMELT2 software (Herzberg and Asimow, 2008) from a MORB glass with Mg# = 70.6 at 0.1 MPa (Table 2). The mantle potential temperature (T_p) calculated for this sample is 1353 °C, very close to the mean T_p of MORB (1350 °C; Courtier et al., 2007). Details of calculations are given in the supplementary material (see supplementary material; Appendix 2 and Table S4). Fig. 11 shows that px-MORBs are too poor in SiO_2 and CaO, and too rich in Al_2O_3 to be explained by fractional crystallization of MPM at 0.1 MPa. With increasing pressure, the fractionated magma becomes poorer in SiO_2 and CaO, and richer in Al_2O_3 and FeO so that the fractionation trends intersect the compositional area of px-MORBs. However, for a given composition, the results require highly contrasting fractionation pressures depending on the oxides under consideration: for example, the SiO_2 and Al_2O_3 contents of px-MORB K10-3 (Fig. 11, Table 2) require a fractionation pressure close to 400 MPa while its FeO and CaO contents require a pressure lower than 100 MPa. Hence, the low SiO_2 contents and the high FeO contents of px-MORBs cannot be explained by fractional crystallization whatever the pressure.

In order to assess if the peculiar features of px-MORBs can result from a deeper melting, we calculated the T_p of each of their compositions with PRIMELT2 assuming a mantle source equivalent to the peridotite DMM1 (Table 2; Wasylenki et al., 2003). This peridotite presents a Mg# (89.9) in the middle of the range expected for peridotites in MORB sources (89.2–90.5; Herzberg and O'Hara, 2002). Fig. 12 presents the distribution of T_p for the whole population of px-MORBs and for each of the eight locations at which px-MORBs were sampled. The T_p range is relatively wide (~100 °C) but more limited within each location, partly due to the small number of data for most locations. Interestingly, the largest temperature interval is between the mean temperatures calculated for samples collected at the East Pacific Ridge (EPR) spreading center (~1515 °C) and on seamounts near EPR (~1435 °C). This observation is consistent with previous geochemical studies (Batiza et al., 1990; Zhang, 2011) that suggest that near-EPR seamounts involve lower degrees of melting and a shallower mantle source than magmas from the EPR.

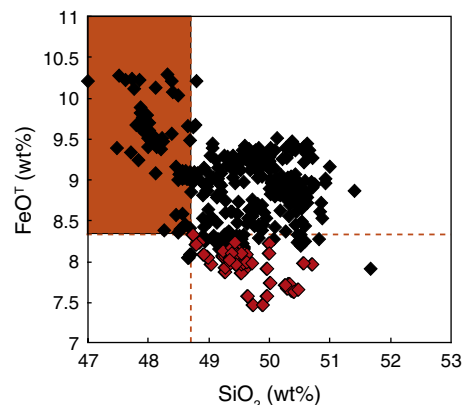


Fig. 10. Total iron contents versus SiO_2 contents for MORB glasses with MgO 9 wt.% in the Melson and O'Hearn's database (2003). Red symbols represent MORB glasses with Mg# 67. The orange rectangle represents the compositional area of px-MORBs, with both lower SiO_2 and higher FeO^T than MORB glasses with Mg# 67.

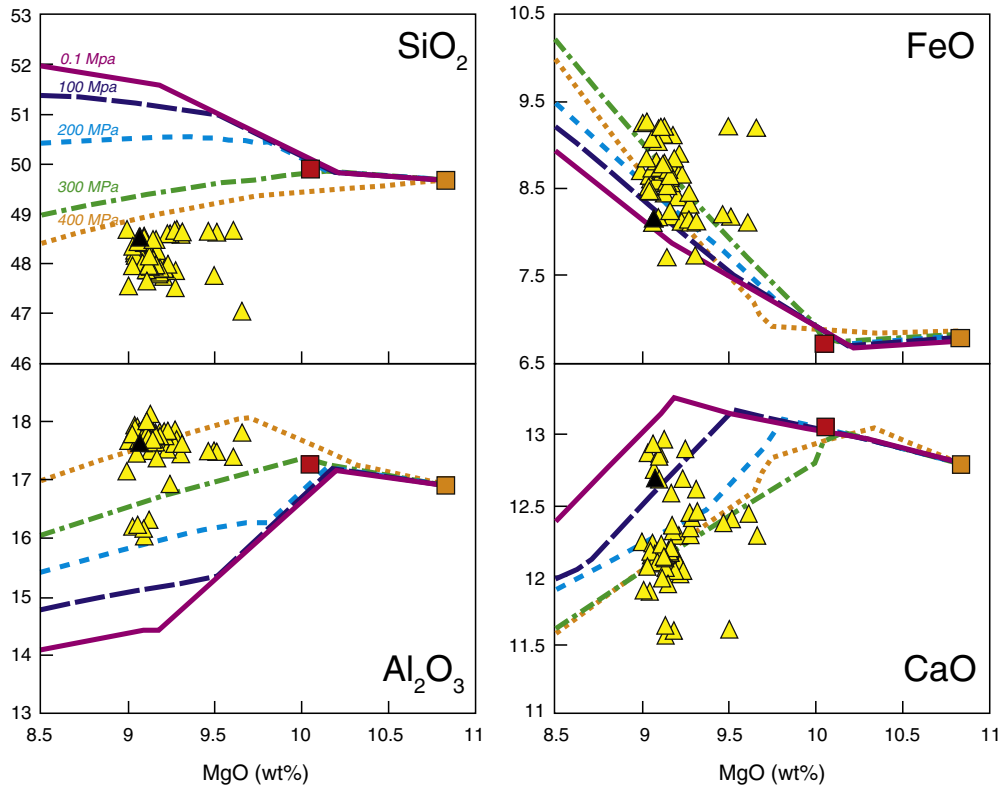


Fig. 11. Plots of SiO_2 , FeO, Al_2O_3 , CaO versus MgO contents for px-MORBs (triangles). Trends of fractional crystallization (Ghiorso and Sack, 1995) of a Model Primary Magma (MPM, orange square; Table S4) at 0.1 MPa (pink), 100 MPa (purple), 200 MPa (blue), 300 MPa (green) and 400 MPa (orange) are shown for comparison. Break in slopes indicates the point at which a fractionating phase is added. From 0.1 to 200 MPa, the order of crystallization is $\text{Ol} \rightarrow \text{Ol} + \text{Plg} \rightarrow \text{Ol} + \text{Plg} + \text{Cpx}$, at 300 MPa, the order is $\text{Ol} \rightarrow \text{Ol} + \text{Plg} + \text{Cpx}$, and at 400 MPa the order is $\text{Pigeonite} \rightarrow \text{Cpx} + \text{Plg}$. The red square represents the composition of the MORB AII107-7 20-3, from which the MPM composition was determined with PRIMELT2 (Herzberg and Asimow, 2008; see Appendix 2 in the supplementary material for details on calculations). The black triangle represents the px-MORB K10-3 (Table 2).

In the same way, spreading centers influenced by hotspots generally present higher potential temperatures than those far from hotspots. For instance, the value of T_p calculated for the Tjörnes Fracture Zone ($\sim 1517^\circ\text{C}$), which is situated just off the northern coast of Iceland, is higher than that for the Mid-Atlantic Ridge (MAR) spreading-center ($\sim 1492^\circ\text{C}$). However, the calculated mean T_p for px-MORBs collected on the Galapagos spreading center ($\sim 1466^\circ\text{C}$) is lower than those calculated for the EPR and the MAR spreading centers. Moreover, the Central Lau spreading center presents also a lower T_p ($\sim 1460^\circ\text{C}$) while T_p beneath back-arc basins are generally slightly higher than beneath mid-ocean ridges (Kelley et al., 2006). Furthermore, according to Wiens et al. (2006), the Lau basin would present the highest T_p of back-arc basins as inferred from seismology, petrology and bathymetry.

Finally, the range of calculated temperatures ($1422\text{--}1525^\circ\text{C}$) is markedly above the average range for MORBs ($1280\text{--}1400^\circ\text{C}$) determined with the same software (Herzberg et al., 2007). We note that this observation remains true for the complete range of peridotites in MORB sources: for instance, if calculations are performed with a fertile peridotite with a low Mg# such as KR4003 (Mg# = 89.2; Walter, 1998), the range of calculated T_p for px-MORBs is $1418\text{--}1500^\circ\text{C}$. Even if thermal anomalies exist at a small scale (e.g., Laubier et al., 2007), the inconsistencies between the calculated T_p and previous estimates, and the very high values of T_p required to explain the enrichment in FeO and the depletion in SiO_2 argue against a generation of px-MORBs by deeper melting of a homogeneous peridotite mantle. Hence px-MORBs remain good candidates for carrying a pyroxenite signature, as suggested by Lambart et al. (2009).

3.1.2. Quantification of the role of pyroxenites

Because peridotites and pyroxenites generate almost similar melt compositions at the P - T conditions expected in mid-oceanic ridge

sources (Lambart et al., 2009), a general quantification of the contribution of pyroxenites from the major-element compositions of MORBs remains problematic. The exercise is easier, however, if we focus on the special case of px-MORBs, which presumably carry the signature of SiO_2 -poor and FeO-rich pyroxenites, such as M7-16 (Table 2), in their source. Below, we try to quantify the contribution of this type of pyroxenites to the generation of these particular basalts.

Fig. 13a presents the evolution of the T_p calculated for px-MORBs as a function of the Mg# value assumed for the mantle: the higher the mantle Mg#, the higher the calculated potential temperature. Assuming $T_p = 1350^\circ\text{C}$ (the mean T_p for MORB), the range of px-MORBs can be explained by a variation of mantle Mg# between 86.5 and 88.6 suggesting that all px-MORB source-regions are enriched in iron. This calculation can be refined by considering the actual T_p prevailing at the eight areas where px-MORBs were collected. In Fig. 13b, the range of Mg# required to explain the px-MORB compositions from a given area is plotted as a function of the T_p estimate for that area (from the literature, see caption of Fig. 13b). With these refined calculations, it appears that px-MORBs from the Central Lau Basin can be explained by the relatively high T_p of the source-region (1449°C ; Wiens et al., 2006) without invoking any iron enrichment of the mantle (Mg# = 89.6). The same observation can be made for a part of the px-MORBs sampled on the Galapagos Spreading Center. Except for these two cases, however, the generation of px-MORBs requires a mantle source with a Mg# lower than the range of Mg# expected for peridotites in MORB sources. Accordingly and if we consider a homogeneous mixture between peridotite DMM1 and the pyroxenite M7-16, the production of px-MORB compositions may require a contribution of up to 17% pyroxenite (beneath the Juan de Fuca ridge; Fig. 13b). Note that this estimate is likely to be a maximum value because, in a mantle

Table 2

Compositions (wt.%) of SD pyroxenite MIX1G^a, SE pyroxenite G2^b, peridotites DMM1^c and HK66^d, primitive MORB All107-7 20-3^e, and px-MORB K10-3^e, the average primitive OIB from Hawaii^f and a high-MgO melilitite^g from Kauai.

	MIX1G	G2	DMM1	HK66	All107-7 20-3	K10-3	Primitive OIB	Melilitite
SiO ₂	45.6	50.1	44.9	48.02	49.89	48.52	49.97	39.79
TiO ₂	0.90	1.97	0.04	0.22	0.62	0.87	2.27	3.42
Al ₂ O ₃	15.2	15.18	2.38	4.88	17.27	17.64	12.53	9.78
Cr ₂ O ₃	0.11	–	0.39	0.25	–	–	–	–
FeO	7.8	9.4	8.3	9.90	7.47	9.06	11.35	14.79
MnO	0.15	0.17	0.13	0.14	–	–	0.18	0.21
MgO	16.67	7.9	41.6	32.35	10.05	9.07	10.95	15.68
CaO	7.48	11.7	2.14	2.97	13.05	12.68	10.06	12.59
Na ₂ O	1.4	3.0	0.055	0.66	1.64	2.11	2.11	2.13
K ₂ O	0.04	0.03	0.006	0.07	0.05	0.05	0.34	0.96
Mg#	79.3	60.1	89.9	85.3	70.6	64.1	65.6	65.4

^a Hirschmann et al. (2003).

^b Pertermann and Hirschmann (2003).

^c Wasylenko et al. (2003).

^d Hirose and Kushiro (1993).

^e Melson and O'Hearn (2003).

^f Jackson and Dasgupta (2008); the average was done on the entire range of compositions between 8 and 16 wt.% MgO.

^g Maaløe et al. (1992).

composed of chemically isolated bodies of pyroxenites into surrounding peridotite, pyroxenites generally produce more melt and have lower solidus temperatures than peridotites. Therefore, the contribution of pyroxenite-derived liquids to total melt production is significantly higher than the proportion of pyroxenites in the source. Lambart et al. (2009) estimated that 2 to 8% of pyroxenites in the source-regions would account for the production of the px-MORBs.

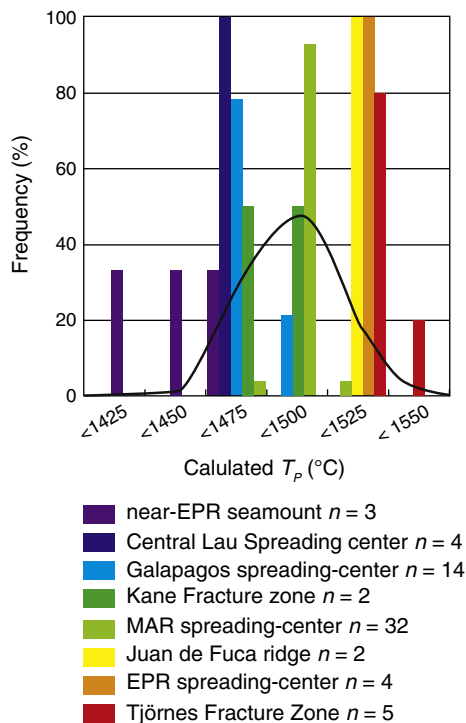


Fig. 12. Frequency of the potential temperatures (T_p) calculated for px-MORBs. Different colors are used for the eight areas where px-MORBs are found: East Pacific ridge (EPR) spreading-center, near-EPR seamounts, Central Lau spreading center, Mid-Atlantic ridge (MAR) spreading center, Kane fracture zone, Tjörnes fracture zone, Juan de Fuca ridge and Galapagos spreading center. The number of samples (n) for each area is given on the figure, showing that about half the px-MORBs come from the Mid-Atlantic ridge. The black curve represents the T_p distribution for all px-MORBs. T_p have been calculated with PRIMELT2 (see Appendix 2 for details on calculations).

3.2. Pyroxenites in OIB source-regions

3.2.1. Pyroxenite versus peridotite major-element signatures

As for MORBs, it has been proposed that major elements can trace a heterogeneous mantle source for OIBs. For instance, Kogiso et al. (1998, 2003) suggested that a pyroxenite contribution is needed to explain the low Al₂O₃ contents, the high FeO contents and the high CaO/Al₂O₃ ratios of some OIBs at a given MgO content. They showed that high pressure (5 GPa) pyroxenite-derived and peridotite-derived partial melts have similar Al₂O₃ contents, but that the former are significantly richer in CaO and poorer in MgO than the latter. Kogiso et al. (2004a) also proposed that the variability of major-element compositions observed in OIBs could partly reflect the contribution of pyroxenitic components: alkalic OIBs would imply the involvement of SD pyroxenites while SE pyroxenites are involved in the genesis of tholeiitic magmas. Prytulak and Elliott (2007) suggested that the high TiO₂ contents of OIBs may also be a marker of pyroxenite contribution. Below, we use experimental data obtained at the P - T conditions expected beneath oceanic islands to evaluate whether the participation of pyroxenite melts can explain the distinguishing features of OIB major-element compositions.

To explore the effects of source heterogeneity on OIB compositions, we consider the case of a heterogeneous mantle composed of interbedded (SE and SD) pyroxenites and peridotites, undergoing adiabatic decompression melting. We ignore chemical and thermal interactions between peridotite and pyroxenite during decompression melting. For a small pyroxenite/peridotite ratio, we can assume that the geothermal gradient is governed by the adiabat of upwelling peridotite (e.g., Hirschmann and Stolper, 1996). Such reasoning was previously used in Lambart et al. (2009) to investigate the role of mantle pyroxenites during MORB genesis. The compositions of partial melts produced by the different rock-types along this adiabatic path are estimated from the experimental database, and then compared to natural compositions of OIBs (Fig. 14). For a given T_p , the final depth of melting strongly depends on the thickness of the lithosphere (e.g., Humphreys and Niu, 2009; Niu et al., 2011).

To limit the effect of this relationship, experimental melts are compared with OIBs from the Hawaii island group which were emplaced on a lithosphere with a constant lithospheric thickness of ~90 km. The well-studied Hawaii volcanoes represent the most productive active mantle plume on Earth. Both silica under-saturated and silica over-saturated magmatic suites, commonly observed in OIBs, are well documented there (Fig. 14). The most voluminous lavas on Hawaii are the tholeiitic shield-stage compositions represented by the orange surrounded dots in Fig. 14. The less abundant Hawaiian alkali

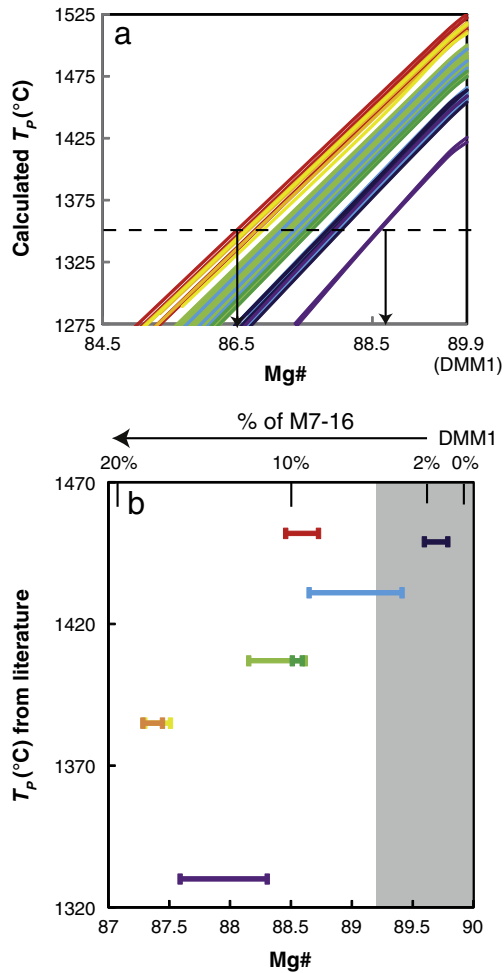


Fig. 13. (a) Potential temperature (T_p) calculated for px-MORBs as a function of the Mg# of the mantle. Each colored line represents a px-MORB (same color scheme as in Fig. 12). The two arrows bracket the range of mantle Mg# required to produce px-MORB compositions assuming $T_p = 1350$ °C (the mean value for MORB). (b) Mg# of the mantle sources required to match the previous estimates of T_p for the eight areas of Fig. 12. The top axis shows the corresponding proportion of pyroxenite M7-16 assuming a homogeneous mix between DMM1 (Mg# = 89.6) and M7-16 (Mg# = 60.6). The gray area represents the range of Mg# expected for peridotites in MORB source-regions (Herzberg and O'Hara, 2002). References are: MAR, Galapagos and EPR spreading centers, and Tjörnes and Kane Fracture Zones, Courtier et al. (2007); Central Lau Spreading center, Wiens et al. (2006); and near-EPR seamount, Batiza et al. (1990). No previous estimate was found for Juan de Fuca Ridge, thus the T_p was considered as equal to the T_p at the EPR spreading center.

compositions (purple surrounded dots in Fig. 14) are mostly post-shield lavas (Moore and Clague, 1992). Many different hypotheses were proposed to explain this compositional variability including a variation of the extent of partial melting (e.g., Ito and Mahoney, 2005), metasomatism of the lithosphere by melts from the underlying asthenosphere (Eggins, 1992), the effect of CO_2 (Dasgupta et al., 2010), or the involvement of various recycled components in the deep mantle source of the plume (e.g., Hauri, 1996; Herzberg, 2006, 2011; Hofmann and White, 1982; Sobolev et al., 2000, 2005). In our calculations, we used the range of T_p of 1520 to 1600 °C calculated by Herzberg and Asimow (2008) with PRIMELT2, assumed that the bottom of the lithosphere (~2.5 GPa) corresponds to the final pressure of melting, and used the parameterization of McKenzie and O'Nions (1991) to determine at a given pressure the actual range of temperatures corresponding to this range of T_p . In this section, we assume that pyroxenite-derived melts may be extracted directly without interaction with neighboring peridotites. This statement and the question of interactions are discussed in Section 3.3.

The average melt compositions from each lithology (SD and SE pyroxenites and peridotites) estimated at different pressures along the adiabatic path are shown in Fig. 14. Note that only stage 1 SE pyroxenites – those directly resulting from the subduction of oceanic crust (see Section 2.2.2) – are considered here; the case of stage 2 SE pyroxenites is discussed in Section 3.4. An important observation in Fig. 14 is while the average MgO content of peridotite melts decreases with pressure, it increases in pyroxenite-derived melts. For peridotites, this decrease is well documented and is due to the presence of Ol as the dominant phase (e.g., Kogiso et al., 2003). In contrast, in pyroxenites, the MgO content is not buffered and simply increases with the melting degree (and thus with decreasing pressure). We observe that the TiO_2 content of melts decreases with decreasing pressure (and with the increase of the mean melting degree). The case of Na_2O is more complicated due to the competition between the decrease of Na compatibility in Cpx with decreasing pressure and the increase of the degree of melting: as a result, the Na_2O content of melts does not change much along the adiabatic path. Overall, the compositional variation of the liquids from stage 1 SE pyroxenites is small because of the high melting degrees undergone by this lithology.

In Fig. 14, compositions of partial melts from peridotites and pyroxenites are compared with natural OIBs and the evolution of liquids derived from peridotites at 4 GPa (close to the solidus) and 2.5 GPa (the assumed final pressure of melting) by fractional crystallization at 10 MPa (e.g., Anderson and Brown, 1993). Low-pressure fractionation of peridotite partial melts can produce liquids with MgO– Al_2O_3 systematics similar to primitive OIBs (MgO > 8 wt.%), but with less TiO_2 and Na_2O than the lavas, with a narrow range of SiO_2 contents compared to the lava range, and cannot reproduce the highest FeO contents and $\text{CaO}/\text{Al}_2\text{O}_3$ ratios observed in alkalic OIBs. An increase of the fractionation pressure would yield lower SiO_2 contents but would be accompanied with an increase of Al_2O_3 and a decrease of the $\text{CaO}/\text{Al}_2\text{O}_3$ ratio due to Cpx crystallization (Fig. 11). On the contrary, as suggested by Kogiso et al. (2003), a large part of the compositional range of alkalic Hawaiian OIBs can be explained by high pressure melting of SD pyroxenites, which produces melts with low Al_2O_3 and high FeO contents, and with high $\text{CaO}/\text{Al}_2\text{O}_3$ ratios. The melting of stage 1 SE pyroxenites could also be involved and be responsible for the high SiO_2 and low FeO contents of tholeiitic OIBs but in this case, a mixture with peridotite partial melts is required to explain the wide range of MgO contents.

Melting of pyroxenites cannot explain the behavior of all elements. Firstly, in contrast to Prytulak and Elliott's assumption (2007), numerous alkalic OIBs have TiO_2 contents too high to be explained only by a pyroxenite contribution. Moreover, as underlined by Herzberg (2006), most tholeiitic lavas are too deficient in CaO to have been formed from a peridotite or a pyroxenite source. Secondly, the very silica depleted compositions (melilitites and nephelinites) mainly sampled on Oahu and Kauai islands (Fig. S7a in the supplementary material), cannot be reproduced either by fractionation of peridotite melts, or by the partial melting of pyroxenites. It is possible that these very silica depleted lavas were generated by partial melting in the presence of CO_2 . Indeed previous experimental studies in the system peridotite $\pm \text{CO}_2$ indicate that melts with SiO_2 content as low as 40 wt.% can be produced by low melting degree (<2%) of a carbonated peridotite (see Appendix 4 in the supplementary material). Furthermore, Dasgupta et al. (2007) showed that TiO_2 behaves as an incompatible element in peridotites at high pressure in the presence of CO_2 , forming very TiO_2 -rich melts at low melt fractions. Consequently, low degree partial melting of carbonated lithologies may explain the formation of the silica-depleted and TiO_2 -enriched end-member of OIBs.

3.2.2. Implications for mantle melting beneath Hawaii during the post-shield phase

Most of the alkalic Hawaiian lavas were formed during the post-shield phase (e.g., Moore and Clague, 1992). The high FeO contents

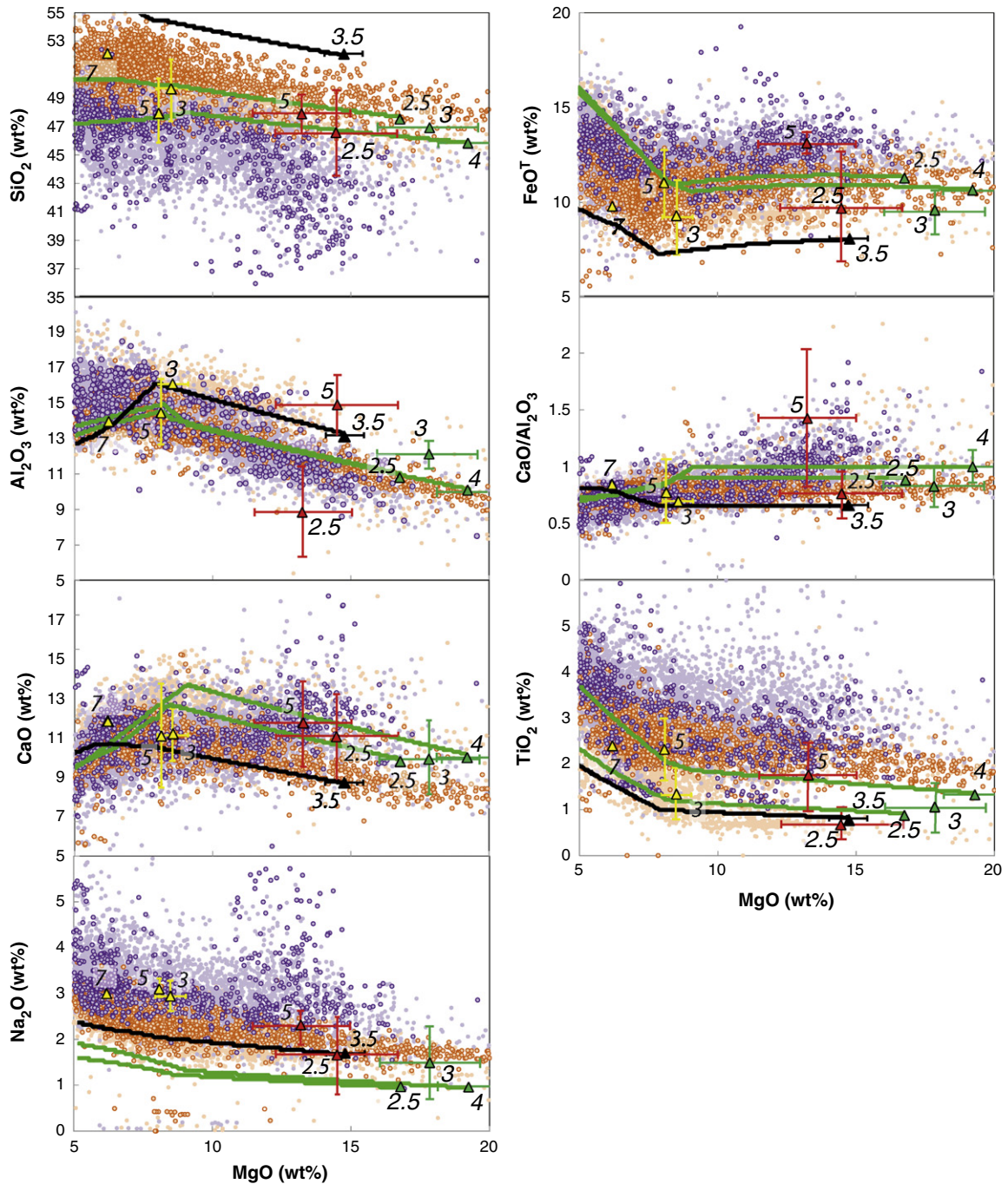


Fig. 14. Major-element compositions of OIBs from Hawaii (surrounded dots) and from other oceanic islands (non-surrounded dots). Purple dots are alkalic compositions and orange dots are tholeiitic compositions according to the definition of Macdonald and Katsura (1964). Lavas are compared to the compositions of average melts from peridotites (green triangles), from SD pyroxenites (red triangles), from stage 1 SE pyroxenites (yellow triangles) and from stage 2 SE pyroxenites (black triangles) produced along an adiabatic path with a range of T_p between 1520 and 1600 °C at various depths, labeled in GPa. At each pressure, the range of temperatures corresponding to this range of T_p has been determined with the parameterization of McKenzie and O'Nions (1991): 1603–1687 °C at 7.5 GPa, 1575–1658 °C at 5 GPa, 1564–1635 °C at 4 GPa, 1530–1567 °C at 3 GPa and 1497–1538 °C at 2.5 GPa. The average melt compositions have been estimated from experimental data. Each triangle represents the mean composition of melts produced at the given pressure for the given lithology. For example, the green triangle with the label “4.0” represents the average composition of melt produced by peridotites at 4 GPa and temperatures between 1564 °C and 1635 °C. The error bar is 1σ . The solid green lines show the trends of fractional crystallization of average melts formed from peridotites at 2.5 and 4 GPa; these trends were calculated at 10 MPa with MELTS (see Appendix 2 in the supplementary material; Ghiorso and Sack, 1995). Data used to estimate the average melt compositions are from Hirose and Kushiro (1993), Kushiro (1996), Takahashi (1986), Takahashi and Kushiro (1983) and Walter (1998) for peridotites, from Hirschmann et al. (2003), Keshav et al. (2004), Kogiso and Hirschmann (2006), Kogiso et al. (2003) and this study for SD pyroxenites, from Pertermann and Hirschmann (2003), Spandler et al. (2008), Yasuda et al. (1994) and Yaxley and Sobolev (2007) for stage 1 SE pyroxenites, and from Sobolev et al. (2007) for the stage 2 SE pyroxenites.

and high $\text{CaO}/\text{Al}_2\text{O}_3$ ratios of these lavas may require both the presence of SD pyroxenites in the source and a high pressure of melting. In fact, the melting of SD pyroxenites produces melts with FeO and $\text{CaO}/\text{Al}_2\text{O}_3$ comparable to the highest contents and ratios of OIBs at a pressure close to 5 GPa. With decreasing pressure, FeO and

$\text{CaO}/\text{Al}_2\text{O}_3$ in the average melt strongly decreases and, at 2.5 GPa, SD pyroxenite and peridotite melts have similar compositions (Fig. 14). Using the experimental data on composition MIX1G (close to the average composition of SD pyroxenites, Table 2; Hirschmann et al., 2003; Kogiso et al., 2003), we attempted to constrain the

potential temperature and final pressure of melting required to keep a mean pressure of melting close to 5 GPa.

We determined the adiabatic melt production of MIX1G using the following procedure: (1) we parameterized the isobaric melt production of MIX1G with a method similar to that used by [Pertermann and Hirschmann \(2003\)](#) on the MORB-type pyroxenite G2 ([Fig. 15a](#) and [Table 2](#); see Appendix 3 in the supplementary material for more details). (2) From this parameterization, we calculated the melt production of MIX1G along adiabats (estimated from the parameterization of [McKenzie and O’Nions, 1991](#)) of various T_p between 1450 and 1600 °C ([Fig. 15b](#)) assuming that the geothermal gradient is governed by the adiabat of upwelling peridotite. This assumption represents the case where the pyroxenite/peridotite ratio tends to zero and the calculated melt production of the pyroxenite is a maximum, as increasing proportions of pyroxenite will cause progressive cooling and reduced melting per increment of upwelling ([Phipps Morgan, 2001](#); [Sleep, 1984](#); [Stolper and Asimow, 2007](#)).

[Langmuir et al. \(1992\)](#) define the mean pressure of melting (P_{mean}) as the average pressure from which the melts are derived. Stated another way, P_{mean} is the pressure at which the melting degree is equal to half the final melting degree undergone by the pyroxenite. Using this definition, we can estimate the P_{mean} of MIX1G for the range of T_p expected beneath Hawaii ([Fig. 15b](#)). For the range of 1520–1600 °C ([Herzberg and Asimow, 2008](#)) and a final pressure of melting, $P_f = 2.5$ GPa [i.e., the asthenosphere–lithosphere boundary (LAB) beneath Hawaii], P_{mean} of MIX1G ranges from 4.06 to 5.15 GPa. [Dasgupta et al. \(2010\)](#) suggested that for islands with a thick lithosphere, melting could stop at a pressure up to 1.5 GPa higher than the pressure at the LAB. For $P_f = 4$ GPa, P_{mean} ranges from 4.42 to 5.17 GPa. In both cases, the estimated T_p to keep $P_{mean} = 5$ GPa is ~1586 °C. Thus our calculations show that the range of T_p expected beneath Hawaii is consistent with a high mean pressure of melting of pyroxenite MIX1G. Note that for a $T_p = 1586$ °C, peridotite is above its solidus between 2.5 and 4.8 GPa and the productivity of the embedded pyroxenite decreases in response to the cooling of the upwelling material needed to supply the heat of fusion of the peridotite. Hence, the mean pressure and the mean degree of melting remain almost constant for P_f between 2.5 and 4 GPa.

The post-shield phase is often considered as the waning stage of magmatism after the Hawaii moved off the “hotspot” center. However, the T_p calculated here is at the high end of the range estimated by [Herzberg and Asimow \(2008\)](#) for the T_p beneath Hawaii. Another possibility to keep a high pressure of melting of MIX1G is that the mantle flux decreased, reducing the extent of decompression melting and thereby favoring the generation an extraction of deeper melt. This is consistent with the high pressure generation of the post-shield lavas estimated by [Lee et al. \(2009\)](#) and with the geochemical and dynamical model of [Farnetani and Hofmann \(2010\)](#).

3.3. Preservation of the pyroxenite signal during melt extraction and transport

If a part of the compositional variability observed in oceanic basalts is actually due to the presence of pyroxenites in their source regions, this requires that pyroxenitic melts are able to transfer their compositional characteristics to erupted basalts. A major unknown is to what extent the chemical signature of pyroxenite-derived liquids can survive the interaction with surrounding peridotites during their transport to the surface.

In many instances and for most major elements, pyroxenite-derived melts are similar to peridotite-derived melts beneath mid-ocean ridges ([Lambart et al., 2009](#)). [Lambart et al. \(2012\)](#) showed that this similarity induces a very limited reactivity between pyroxenite-derived melts and the surrounding peridotite. As discussed in [Section 3.1](#), however, MORBs that are likely to carry a pyroxenitic signature in their major-element composition require the contribution of liquids derived from (Gt–Ol) clinopyroxenites like M7-16. These clinopyroxenites

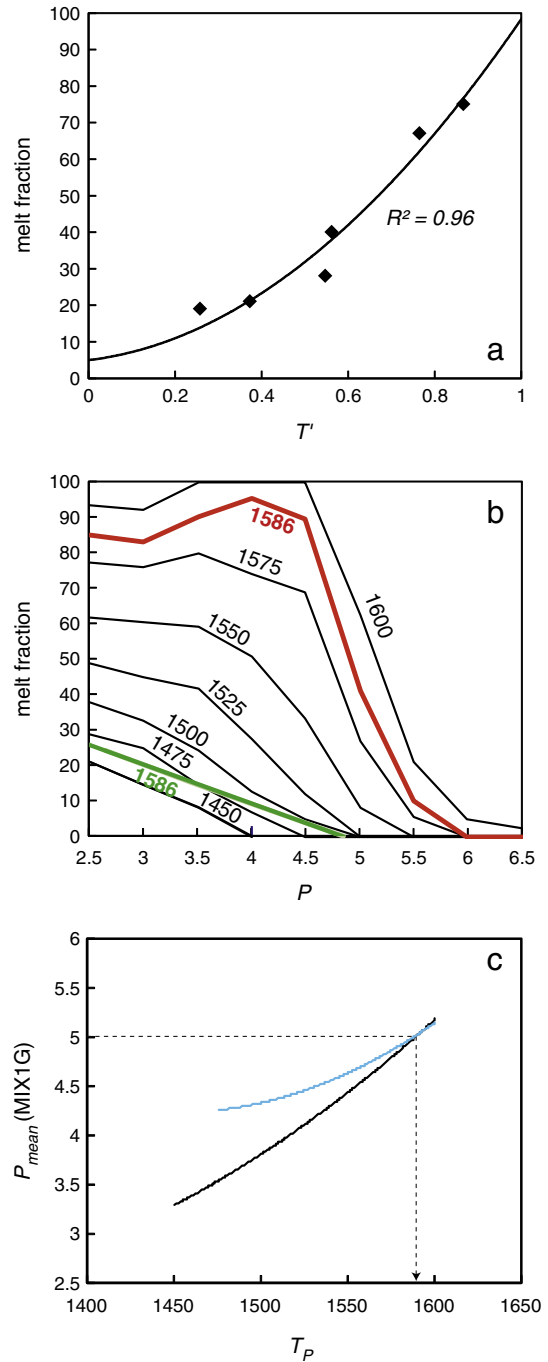


Fig. 15. (a) Melt fraction (F) from the MIX1G partial melting experiments ([Hirschmann et al., 2003](#); [Kogiso et al., 2003](#)) plotted against scaled temperature T' (diamonds), defined as $T' = (T - T_{5\%}) / (T_{liq} - T_{5\%})$ with $T_{liq} = 1343 + 73.6P$ (GPa) and $T_{5\%} = 1196 + 86.7P$ (GPa), and compared to the fitted trend (black curve) given by $F = a \cdot T'^2 + b \cdot T' + 5$, where $a = 79.23$ and $b = 14.13$. (b) Calculated melt fraction along adiabats for various T_p labeled in °C (black and red curves). Adiabats are estimated from the parameterization of [McKenzie and O’Nions \(1991\)](#) and melt productivity is taken from parameterization described above. The melt fraction of a garnet peridotite calculated from the parameterization of [McKenzie and O’Nions \(1991\)](#) for $T_p = 1586$ °C is shown for comparison (green line). (c) Mean pressure of melting of MIX1G, (P_{mean}), as a function of the potential temperature (T_p) for final pressure of melting of 2.5 GPa (black curve) and 4 GPa (blue curve). The arrow indicates the T_p required to keep $P_{mean} = 5$ GPa.

produce liquids strongly depleted in SiO_2 and enriched in FeO in comparison with peridotite-derived melts.

Two cases must be distinguished depending on whether the neighboring peridotites are above or below their solidus ([Lambart et al.,](#)

2012). If the surrounding mantle is partially molten, the pyroxenite-derived melts can be extracted from their source but, if melt transport is by porous flow, they will undergo significant chemical changes during their transport, in particular a strong silica enrichment and an iron depletion, and lose their specific signature. If the surrounding mantle is subsolidus, the melts will react with Opx and be consumed to produce Ol + Cpx + Gt (see below). The situation is different, however, if melt transport is by focused flow in dunite channels (Kelemen et al., 1995). In this situation, pyroxenite melts may preserve a part of their specific signature: the liquid should equilibrate with the surrounding dunite (Mg# 91; Braun and Kelemen, 2002) and loses its low Mg# signature (partly or totally depending on the magma/rock ratio) whereas other chemical features, such as a low-SiO₂ or high CaO/Al₂O₃, should remain unchanged. There is a consensus that such conduits exist at low pressure but it is less clear whether they exist at greater depths. On the other hand, Opx may be absent from near-solidus peridotite above 3 GPa (Walter, 1998), so partial melts of Gt-pyroxenites produced at $P > 3$ GPa may not be significantly affected by melt–rock reactions. Finally, all compositional signatures (low Mg#, low-SiO₂, high CaO/Al₂O₃) may be preserved if pyroxenite-derived liquids are transported in dikes, but such a mechanism would presumably require that pyroxenites occur as large isolated bodies in the heterogeneous mantle (Kogiso et al., 2004b).

Except in the cases of melt transport in dunite channels or in dikes, pyroxenite-derived melts should not escape significant interaction with the surrounding peridotites. The importance of such interactions for the production of oceanic basalts and the possibility that the pyroxenite signal survives these interactions are discussed in the next section.

3.4. Importance of pyroxenite–peridotite interactions in the genesis of oceanic basalts

Melt–rock interactions, particularly those between pyroxenite-derived melts and peridotites, play an important role in the chemical transformation of upper mantle rocks and in basalt genesis. For instance, such interactions have been invoked to explain isotopic systematics and major and trace element compositions of abyssal peridotites (e.g., Brunelli and Seyler, 2010; Seyler et al., 2003, 2004; Suhr et al., 2008; Warren and Shimizu, 2010) and the formation of new compositional and lithological heterogeneities in ultramafic massifs and in xenoliths (e.g., Ackerman et al., 2009; Garrido and Bodinier, 1999; Marchesi et al., 2011; Mazzucchelli et al., 2009; Porreca et al., 2006; Sen et al., 2011). Two main types of models have been proposed to evaluate the role of pyroxenite–peridotite interactions in basalt genesis: (1) a “direct interaction model” in which the composition of the pyroxenite-derived melt progressively changes by reaction with the surrounding peridotite. For instance, Pilet et al. (2008) and Mallik and Dasgupta (2012) suggested that the compositional range of OIBs is produced by interaction between peridotites and melts coming from either a hydrous SD pyroxenite or a stage 1 SE pyroxenite, respectively. (2) An “indirect interaction model” which initially requires the formation of a stage 2 pyroxenite by reaction between the initial pyroxenitic melt and the peridotite, followed by partial melting of this stage 2 pyroxenite. For instance, on the basis of the high Ni content of olivines and melts, Sobolev et al. (2005, 2007) proposed that the Hawaiian shield basalts were produced by partial melting of Ol-free, stage 2 pyroxenites resulting from the interactions between eclogite-derived melts (stage 1 SE pyroxenites) and peridotites. Below, we discuss these two melt–rock interaction models from the literature.

3.4.1. Direct interaction model

The wide range of SiO₂ contents in OIBs cannot be reproduced by partial melting of a homogeneous mantle and seems to require the involvement of various types of pyroxenite lithologies in addition to

peridotites in the source-regions (Fig. 14). Mallik and Dasgupta (2012) proposed a model in which partial melts from a single stage 1 SE pyroxenite (a MORB-eclogite) interact with a fertile peridotite: variations of the melt–rock ratio yields a range of reacted melts that can explain the transition from alkalic to tholeiitic compositions observed in OIBs; liquids matching the composition of near-primary OIBs (MgO-rich, high TiO₂ and Na₂O) are produced at 3 GPa and temperatures between 1375° and 1440 °C. These temperatures are below those expected beneath oceanic islands at this pressure (1481–1567 °C; Herzberg and Asimow, 2008). On the basis of the good agreement between the compositions of their experimental melts at 3 GPa and 1375 to 1440 °C and near-primary OIBs, Mallik and Dasgupta (2012) suggested that current estimates of mantle T_p beneath oceanic islands may be overestimated: a T_p of ~1350 °C, close to the mean T_p of MORB, would be sufficient. If such low T_p may hold in the case of some weak plumes or at the edges of strong plumes, the absence of thermal anomaly is hardly consistent with geophysical observations at many oceanic islands, especially in the case of Hawaii where an excess temperature of the asthenosphere of 200° to 300 °C is generally accepted (Constable and Heinson, 2004; Laske et al., 1999; Sleep, 1990).

A major unknown in the direct interaction model, whatever the kind of pyroxenite involved, is the ability of the initial melt to infiltrate deeply into and react with the adjacent peridotite and then to be extracted from the peridotite, in particular when the latter is subsolidus. The reaction between stage 1 SE pyroxenite melt and peridotite precipitates Opx at the expense of Ol, as observed in the products of the layered experiments of Mallik and Dasgupta (2012), in which the melt layer is separated from the lherzolitic residual mineral assemblage by a reaction zone comprising Opx + Cpx + Gt. The reaction between a SD pyroxenite melt and a subsolidus peridotite has not been investigated experimentally at high pressure (> 2 GPa). However, Lambart et al. (2012) performed thermodynamical calculations of the interaction between two different SD pyroxenite melts (from runs #P16-25 and #P40-25 in Table 1) and a subsolidus peridotite at 2.5 GPa.

The reaction of these melts with the subsolidus mantle results in strong melt consumption and substantial Cpx production. Considering a pyroxenite body surrounded by peridotite, the interaction reaction is thus likely to occur only at a small scale along the interface between the two rock-types, leading to the development of a low permeability barrier around the pyroxenite body and favoring a (near) closed-system evolution of the partially molten pyroxenite. Mechanical destabilization of this melt-rich body could allow rapid melt transport to the surface (Kogiso et al., 2004b) thus providing an efficient mechanism for extracting the liquid without interaction with the surrounding mantle. Considering the limited extent of pyroxenite–peridotite interactions expected in natural systems, the mechanisms that can produce and extract a full range of liquids by varying the ratio of pyroxenitic melt to peridotite, as suggested by Mallik and Dasgupta (2012), remain unclear.

3.4.2. Indirect interaction model: formation of stage 2 pyroxenites from SE and SD pyroxenite-derived melts

Primary magmas of the Hawaiian tholeiites (shield stage) have been estimated by a variety of different methods: in most cases, they show high SiO₂ contents (e.g., Hauri, 1996; Herzberg, 2011; Stolper et al., 2004). As underlined in Section 3.2.1, the direct participation of melts derived from stage 1 SE pyroxenites could explain the high silica content of Hawaiian tholeiitic lavas, but these melts are too poor in MgO to represent their parental magmas. Sobolev et al. (2005) suggested that the Hawaiian tholeiites were produced by the partial melting of stage 2 pyroxenites. Sobolev et al. (2007) performed experiments at 3.5 GPa on a model stage 2 Ol-free pyroxenite (Px-1) produced by the reaction between 55% stage 1 SE pyroxenite-derived melt and 45% peridotite.

In Fig. 14, we report the average melt produced by Px-1 at 3.5 GPa along an adiabatic path with $T_p = 1520\text{--}1600\text{ }^\circ\text{C}$ (the range of T_p suggested by Herzberg and Asimow, 2008). The average melt is MgO-rich (14.7 wt.%) and we observe that low pressure differentiation of the stage 2 Ol-free SE pyroxenite melt (black curve) can explain the low CaO content (Herzberg, 2006) and the Na₂O content of the tholeiitic lavas. The silica content of the differentiated melt is, however, too high, and the FeO and TiO₂ contents are too low, in comparison to natural lavas. We note that these discrepancies may be due to the lack of experimental data on stage 2 SE pyroxenites as the only available data are those from Sobolev et al. (2007) on composition Px-1 at 3.5 GPa. Herzberg (2006) estimated the composition of a model primary magma of high SiO₂ Hawaiian lavas. This primary magma is poorer in SiO₂ (48.6–49.5 wt.%) and richer in TiO₂ (1.8–2%) than the melts derived from Px-1, and may be formed by a stage 2 SE pyroxenite (Opx + Cpx + Gt) produced by reacting low degree melts of stage 1 SE pyroxenite with peridotite. Hence Hawaii is likely to be a good example for the participation of stage 2 SE pyroxenites in basalt generation.

There are no experimental data on the formation of stage 2 SD pyroxenites but calculations performed by Lambart et al. (2012) on the interaction between two different SD pyroxenite melts (from runs #P16-25 and #P40-25 in Table 1) and a subsolidus peridotite at 2.5 GPa illustrate the types of stage 2 SD pyroxenites that could be produced. The #P16-25 melt has a low SiO₂ and a high FeO content with a high CaO/Al₂O₃ ratio (1.2). These are the three main compositional characteristics for the presence of pyroxenite in the source-regions (see above). For a 1:1 melt–rock ratio, the mineralogical mode obtained at the end of the reaction is wehrlitic, with 49.5% Ol, 44.6% Cpx and 5.9% Gt.

The composition of the #P40-25 pyroxenite melt is richer in silica (but still on the SD side of the thermal divide; Fig. 7) and very rich in alkalis. Interaction between this melt and the subsolidus peridotite at 2.5 GPa produce Cpx, Opx and Gt and dissolve Ol; the resulting mineral assemblage for a 1:1 ratio is an Ol-websterite composed of 16.8 wt.% Ol, 40.3% Cpx, 17.9% Opx and 10.8% Gt. Although their phase proportions are very different, hybrid Ol-websterites produced in the case of melt P40-25 and peridotites have the same phase assemblage (Ol + Opx + Cpx + Gt or Sp depending on pressure). Consequently, the melting reactions will be similar (Lambart et al., 2009). With decreasing pressure, the melting reaction is expected to change from Ol + Cpx + Gt = Opx + Liq to Opx + Cpx + Sp = Ol + Liq (Walter, 1998). Therefore, the silica content of the partial melt should strongly increase with decreasing pressure in response both to increasing degree of melting (Walter, 1998) and to the change of melting reaction that causes the consumption of Opx.

Conversely, the melting reaction of the Opx-free wehrlite produced in the case of melt P16-25 is expected to be Cpx + Gt + Ol = Liq (see Appendix 1 in the supplementary material; Fig. S4). This reaction will produce very SiO₂-poor melts due to the absence of Opx (Lambart et al., 2009). Moreover, due to the Ol buffering effect, the FeO content should not vary a lot (e.g., Médard et al., 2006) and remains relatively high. Finally, the presence of Gt in the residual assemblage results in a compatible behavior of Al₂O₃ and therefore this hybrid lithology should produce liquids with relatively high CaO/Al₂O₃ ratios. Consequently, partial melting of these secondary wehrlites is likely to produce melts with the same major-element characteristics than the initial pyroxenitic melt (#P16-25), thus preserving the original pyroxenite signature despite important melt–rock interactions. We note that with a lower ratio of melt P16-25 to peridotite, Opx is present in the residual assemblage (Lambart et al., 2012). In this case, the melting behavior is similar to Ol-websterites (or peridotites). The silica enrichment should remain very limited, however, because (1) the initial silica content of the hybrid pyroxenite is low, and (2), in the presence of Gt, the amount of Opx produced at high pressure during melting is small (Walter, 1998). Thus, during decompression, when Opx switches from the product side to

the reactant side of the melting reaction, it is consumed, and the melting reaction reverts to Cpx + Ol ± Gt = Liq. Consequently, the transfer of the major-element pyroxenite signature to the basalt composition via a secondary, hybrid pyroxenite seems possible even at low melt–rock ratios in the case of SD pyroxenite, whereas it requires the complete suppression of Ol in the hybrid assemblage in the case of SE pyroxenites, and thus high melt–rock ratios.

The interaction between a pyroxenite liquid and a peridotite can give rise to a large variety of stage 2 pyroxenites that can produce MgO-rich liquids carrying, at least in some cases, the major-element signature of the initial pyroxenitic liquid. Sobolev et al. (2005, 2007) has emphasized the importance of stage 1 SE pyroxenites (as eclogites from recycled oceanic crust) as the source of the interacting liquid. We propose that this model can be extended to all pyroxenites (SD and SE). Depending on the initial melt, melt–rock interactions yield various types of stage 2 pyroxenites, which generate upon decompression a range of liquids that reproduces the compositional variability of OIBs.

3.5. Nature of pyroxenites in the source of oceanic basalts and the origin of SD pyroxenites

In experimental studies, two approaches have been used to estimate the composition of “mantle heterogeneities”: the analog method and the forward method (Kogiso et al., 2004a). These two methods differ on many points and have been widely debated. Although some models favor a single mafic composition (namely MORB-eclogite) in mantle sources, both the analog and forward approaches point to a wide range of pyroxenite compositions potentially present in the source-regions of basalts, reflecting various origins and various degrees of interaction with peridotites.

In the analog approach, the composition of pyroxenites in mantle sources is estimated from studies of natural, mafic rock-types sampled as xenoliths in lavas or as layers and lenses in tectonically exhumed ultramafic massifs and ophiolites. The main limitation with this method is that most of these samples (Figs. 1, 2) come from the lithosphere and not from the convective mantle, the predominant source of oceanic magmas. Accordingly, these natural pyroxenites may have been modified by lithospheric processes such as metasomatism or partial melting at low pressures, and therefore may not be representative of pyroxenites in the convecting mantle (e.g., Kelemen et al., 1997). Nevertheless, they can be introduced into the deeper mantle when lithospheric regions are subducted or delaminated (Pilet et al., 2005, 2008, 2011).

The forward method aims at estimating what are the likely compositions of pyroxenites in the mantle sources of basalts on the basis of models of mantle pyroxenite formation and evolution. Assumptions must be made on how pyroxenitic rocks are incorporated into the convecting mantle, what are their initial compositions, what kind of chemical and mineralogical changes they undergo during their transport, etc. In this approach, subduction of the oceanic crust is often chosen as the major process of pyroxenite formation, and the composition of the subducted crust is equated to that of modern MORB modified by alteration on the sea floor and by mass transport processes in subduction zones (e.g., Pertermann and Hirschmann, 2003; Spandler et al., 2008; Yasuda et al., 1994). The resulting pyroxenites are silica-excess eclogites at upper mantle conditions.

In addition to MORB, however, the oceanic crust also consists of cumulates of dunites, troctolites and Ol-gabbros, most of which are MgO-rich and will produce Ol-bearing, SD pyroxenites after recycling into the upper mantle (Herzberg et al., 2007). Evidence for the participation of such materials in the Hawaiian mantle sources was given by Sobolev et al. (2000). In the same vein, Herzberg (2011) suggested that a very wide range of whole-rock pyroxenite compositions can be formed by solid-state reaction between a MORB and a peridotite depending on depth: while this reaction produces SE pyroxenites in the upper mantle, it produces silica-deficient assemblages in the lower mantle, with Mg- and Ca-perovskite (MgPv and CaPv) and a

silica-poor, sodium-rich aluminous phase ($\text{NaAlSi}_3\text{O}_8$) with a calcium ferrite structure (CF; Fig. 2). Such assemblages can be incorporated into a rising mantle plume, return to the upper mantle, and form Ol-bearing pyroxenites ($\text{MgPv} + \text{CaPv} + \text{CF} = \text{Ol} + \text{Cpx} + \text{Gt}$).

As discussed above, the contribution of iron-rich and silica-poor SD pyroxenites could explain a large part of the oceanic basalt variability not reproduced by the partial melting of peridotites. The origin of these rocks remains controversial, however, and their role in the source-regions of basalts is debated (e.g., Warren and Shimizu, 2010). We have already mentioned two mechanisms able to generate SD pyroxenites: recycling of MORB into the lower mantle (or the boundary layer) and then back into the upper mantle, and delamination of troctolite and gabbro cumulates into the upper mantle. A third mechanism, especially suited to generate iron-rich and silica-poor SD pyroxenites, comes from the work of Pilet et al. (2005, 2008, 2010, 2011). They suggested that dehydrated equivalents of amphibole-rich, metasomatic veins, interpreted as cumulates produced by crystallization of low-degree melts of the underlying asthenosphere, can play a major role in the genesis of alkaline OIBs. This assumption, which is consistent with the isotopic heterogeneity observed in the source of oceanic basalts (Pilet et al., 2005), allowed the authors to explain the very silica depleted compositions of OIBs. Pilet et al. (2008) performed experiments at 1.5 GPa on a hornblende (AG4; Table S1 in the supplementary material) and its dehydrated equivalent, and showed that these compositions produce melts with very low silica (<40 wt.%) and high FeO contents (up to ~16 wt.%). Compositions of hornblendites from ultramafic massifs and xenoliths collections are reported in Fig. 1: pyroxenite M7-16 falls in the field of hornblendites but presents lower TiO_2 and alkali contents. Thus compositions like M7-16 may represent metasomatic veins formed by crystallization of low-degree, hydrous peridotite melts, and subsequently depleted in incompatible elements by a melt extraction event. Further experimental investigations are needed to support this assumption, but metasomatism of the oceanic lithosphere followed by dehydration during subduction may therefore be a likely scenario for the formation of a silica-poor and iron-rich pyroxenitic component in the source-regions of oceanic basalts.

4. Summary points

1. The pressure, at which the thermal divide, defined by the aluminous pyroxene plane in the CMAS system becomes effective, depends on the bulk composition. It is slightly lower than 3 GPa in the CMAS system and decreases with increasing FeO and TiO_2 contents. For most natural pyroxenites, the thermal divide appears to be effective at 2 GPa. The thermal divide separates pyroxenites in two classes with contrasting high pressure melting phase relations (Fig. 2): silica-deficient pyroxenites, which plot and produce liquids on the SiO_2 -poor side of the thermal divide, and silica-excess pyroxenites, which plot and produce liquids on the SiO_2 -rich side of the divide. As a result, liquids from SD pyroxenites tend to be richer in MgO and to a lesser extent in FeO, and poorer in SiO_2 than those of SE pyroxenites. Melt compositions are, however, strongly influenced by non-CMAS elements (especially FeO, TiO_2 , Na_2O and K_2O) and no sharp barrier exists between melts from SE and SD pyroxenites. For instance, liquids with up to 52 wt.% SiO_2 can be produced at low degrees of melting of SD pyroxenites.
2. The demonstration that pyroxenites are present in the source of oceanic basalts on the basis of major-elements is a delicate exercise because, at identical pressure and temperature conditions, many pyroxenites produce melts that are similar in many aspects to peridotite-derived melts. Due to the higher melting degrees experienced by pyroxenites compared to peridotites, pyroxenite-derived melts are usually not enriched in incompatible elements despite the higher concentrations of those elements in the bulk rock. Beneath oceanic islands, peridotites, SD pyroxenites and SE pyroxenites

produce melts with strongly contrasting MgO contents, but this cannot be directly used as a marker for the presence of pyroxenites in the source-regions because it is very sensitive to differentiation by magma-rock interaction. Finally, the more reliable markers for the presence of pyroxenites in the source of oceanic basalts are a low SiO_2 content and a high FeO content of the latter; a third marker is a high $\text{CaO}/\text{Al}_2\text{O}_3$ ratio in the case of OIBs. Only the few pyroxenite types able to impart this signature to the magma can be identified on the basis of the major-element compositions of basalts: other pyroxenite types may be present in the heterogeneous mantle, but they will hardly be detectable in the major-element patterns.

3. Several recent studies have proposed a model of heterogeneous mantle with only one component (MORB-eclogite) in addition to peridotite (Dasgupta et al., 2010; Mallik and Dasgupta, 2012; Sobolev et al., 2005, 2007), leading to very strong constraints on melt compositions and/or mantle potential temperatures. A wide range of pyroxenites is however, expected to be present in the upper mantle. This is supported by: (i) mass-balance calculations showing that solid-state reaction between MORB and peridotite can produce almost the whole range of pyroxenite compositions reported in the literature; and (ii) petrological, geochemical, thermodynamical and experimental data that highlight the formation of new lithological heterogeneities by melt-rock interaction in various geodynamical contexts.
4. One argument against the participation of pyroxenites in basalt genesis is the relatively low MgO contents of most pyroxenite melts (Fig. 7) in comparison to primary magmas of oceanic islands (10–20 wt.%). Interaction processes could account for this apparent paradox: the reaction between pyroxenite-derived melts and surrounding peridotites may indeed form new hybrid rock-types, which are able to produce high MgO magmas and which may preserve, in some cases, the pyroxenite signature of the original melt. The role of solid state and melt-rock reactions in the mantle could therefore be crucial in the genesis of oceanic basalts. However, few studies have been focused on the formation of these pyroxenites of second generation. A direction for future research is to produce forward models of possible stage 2 pyroxenite compositions, and to experimentally determine the composition of melts derived from these compositions. Further work is also required to determine the ability of pyroxenite-derived melts to infiltrate deeply into and react with peridotites, and the conditions under which the pyroxenitic signature may be transferred to basalts despite important melt-rock interactions.
5. Partial melting of volatile-free peridotites or pyroxenites cannot explain the very silica depleted compositions ($\text{SiO}_2 < 42$ wt.%) and the high TiO_2 contents of some OIBs. The protoliths of such compositions are either carbonated lithologies (pyroxenites or peridotites) or metasomatic veins (formed in the lithosphere by crystallization of low-degree, hydrous peridotite melts). The distinction between these two hypotheses cannot be made only on the basis of the major-element compositions of basalts.

Supplementary data to this article can be found online at <http://dx.doi.org/10.1016/j.lithos.2012.11.018>.

Acknowledgements

We are grateful to Andrew Kerr for inviting us to write this review article. We thank Jacques Kornprobst, Emeritus Professor at Université Blaise Pascal, Clermont-Ferrand, for providing the two pyroxenites from Beni Bousera used in this study. Special thanks are also due to the following persons: Jean-Louis Fruquière and Frank Pointud for manufacturing the piston-cylinder assemblages and for maintenance operations, and Jean-Luc Devidal and Chi Ma for technical assistance with the electron microprobes. This study has benefited from discussions with Paul Asimow, Mike Baker, Edward Stolper,

Marion Le Voyer and Christophe Brosson. This is Laboratory of Excellence ClerVolc contribution no. 46. This work was also supported by the program DyETI of the Institut National des Sciences de l'Univers (INSU-CNRS), by the Agence Nationale de la Recherche MIME grant (ANR-07-BLAN-0130-01 to A. Provost), and by the National Science Foundation grant EAR-9528594. We also thank Claude Herzberg and an anonymous reviewer for their constructive reviews.

References

- Ackerman, L., Jelinek, E., Medaris Jr., G., Ježek, J., Siebel, W., Strnad, L., 2009. Geochemistry of Fe-rich peridotites and associated pyroxenites from Horní Bory, Bohemian Massif: insights into subduction-related melt–rock reactions. *Chemical Geology* 259 (3–4), 152–167.
- Albarède, F., Provost, A., 1977. Petrological and geochemical mass-balance equations: an algorithm for least-square fitting and general error analysis. *Computers and Geosciences* 3 (2), 309–326.
- Allègre, C.J., Turcotte, D.L., 1986. Implications of a two-component marble-cake mantle. *Nature* 323 (6084), 123–127.
- Allègre, C.J., Schiano, P., Lewin, E., 1995. Differences between oceanic basalts by multitrace element ratio topology. *Earth and Planetary Science Letters* 129, 1–12.
- Ancey, M., Bastenaire, F., Tixier, R., 1978. Application des methodes statistiques en microanalyse. In: Maurice, F., Meny, L., Tixier, R. (Eds.), *Les éditions du physicien*, Orsay, pp. 323–347.
- Anderson, A.T., Brown, G.G., 1993. CO₂ and formation pressures of some Kilauean melt inclusions. *American Mineralogist* 78, 794–803.
- Arculus, R.J., Johnson, R.W., Chappell, B.W., McKee, C.O., Sakai, H., 1983. Ophiolite-contaminated andesites, trachybasalts, and cognate inclusions of Mount Lamington, Papua New Guinea: anhydrite-amphibole-bearing lavas and the 1951 cumulodome. *Journal of Volcanology and Geothermal Research* 18 (1–4), 215–247.
- Asimow, P.D., Langmuir, C.H., 2003. The importance of water to oceanic mantle melting regimes. *Nature* 421, 815–820.
- Asimow, P.D., Hirschmann, M.M., Stolper, E.M., 2001. Calculation of peridotite partial melting from thermodynamic models of minerals and melts. IV. Adiabatic decompression and the composition and mean properties of mid-ocean ridge basalts. *Journal of Petrology* 42 (5), 963–998.
- Baker, M.B., Stolper, E.M., 1994. Determining the composition of high-pressure mantle melts using diamond aggregates. *Geochimica et Cosmochimica Acta* 58 (13), 2811–2827.
- Baker, M.B., Hirschmann, M.M., Ghiorso, M.S., Stolper, E.M., 1995. Compositions of near-solidus peridotite melts from experiments and thermodynamic calculations. *Nature* 375 (6529), 308–311.
- Batiza, R., Niu, Y., Zayac, W.C., 1990. Chemistry of seamounts near the East Pacific Rise: implications for the geometry of subaxial mantle flow. *Geology* 18, 1122–1125.
- Blichert-Toft, J., Albarède, F., Kornprobst, J., 1999. Lu–Hf isotope systematics of garnet pyroxenites from Beni Bousera, Morocco: implications for basalt origin. *Science* 283 (5406), 1303–1306.
- Bonatti, E., 1990. Not so hot “hotspots” in the oceanic mantle. *Science* 250, 107–111.
- Braun, M.G., Kelemen, P.B., 2002. Dunite distribution in the Oman ophiolite: implications for melt flux through porous dunite conduits. *Geochemistry, Geophysics, Geosystems* 3 (11). <http://dx.doi.org/10.1029/2001GC000289>.
- Brunelli, D., Seyler, M., 2010. Asthenospheric percolation of alkaline melts beneath the St. Paul region (Central Atlantic Ocean). *Earth and Planetary Science Letters* 289, 393–405.
- Chase, C.G., 1981. Oceanic island Pb: two stage histories and mantle evolution. *Earth and Planetary Science Letters* 52, 277–284.
- Constable, S., Heinson, G., 2004. Hawaiian hot-spot swell structure from seafloor MT sounding. *Tectonophysics* 389, 111–124.
- Courtier, A.M., Jackson, M.G., Lawrence, J.F., Wang, Z., Lee, C.-T.A., Halama, R., Warren, J.M., Workman, R., Xu, W., Hirschmann, M.M., Larson, A.M., Hart, S.R., Lithgow-Bertelloni, C., Stixrude, L., Chen, W.-P., 2007. Correlation of seismic and petrologic thermometers suggests deep thermal anomalies beneath hotspots. *Earth and Planetary Science Letters* 264 (1–2), 308–316.
- Dasgupta, R., Hirschmann, M.M., 2010. The deep carbon cycle and melting in Earth's interior. *Earth and Planetary Science Letters* 298, 1–13.
- Dasgupta, R., Hirschmann, M.M., Smith, N.D., 2007. Partial melting experiments of peridotite + CO₂ at 3 GPa and genesis of alkalic ocean island basalts. *Journal of Petrology* 48 (11), 2093–2124.
- Dasgupta, R., Jackson, M.G., Lee, C.-T.A., 2010. Major element chemistry of ocean island basalts conditions of mantle melting and heterogeneity of mantle source. *Earth and Planetary Science Letters* 289, 377–392.
- Davis, F.A., Hirschmann, M.M., Humayun, M., 2011. The composition of the incipient partial melt of garnet peridotite at 3 GPa and the origin of OIB. *Earth and Planetary Science Letters* 308 (3–4), 380–390.
- Day, J.M.D., Pearson, D.G., Macpherson, C.G., Lowry, D., Carracedo, J.-C., 2009. Pyroxenite-rich mantle formed by recycled oceanic lithosphere: oxygen–osmium isotope evidence from Canary Island lavas. *Geology* 37 (6), 555–558.
- Downes, H., 2007. Origin and significance of spinel and garnet pyroxenites in the shallow lithospheric mantle: ultramafic massifs in orogenic belts in Western Europe and NW Africa. *Lithos* 99, 1–24.
- Eason, D., Sinton, J., 2006. Origin of high-Al N-MORB by fractional crystallization in the upper mantle beneath the Galápagos Spreading Center. *Earth and Planetary Science Letters* 252, 423–436.
- Eggs, S.M., 1992. Petrogenesis of Hawaiian tholeiites: 1, phase equilibria constraints. *Contributions to Mineralogy and Petrology* 110, 387–397.
- Falloon, T.J., Danyushevsky, L.V., 2000. Melting of refractory mantle at 1.5, 2 and 2.5 GPa under anhydrous and H₂O-undersaturated conditions: implications for the petrogenesis of high-Ca boninites and the influence of subduction components on mantle melting. *Journal of Petrology* 41 (2), 257–283.
- Falloon, T.J., Green, D.H., Danyushevsky, L.V., McNeill, A.W., 2008. The composition of near-solidus partial melts of fertile peridotite at 1 and 1.5 GPa, implications for the petrogenesis of MORB. *Journal of Petrology* 49 (4), 591–616.
- Farnetani, C.G., Hofmann, A.W., 2010. Dynamics and internal structure of the Hawaiian plume. *Earth and Planetary Science Letters* 295 (1–2), 231–240.
- Gaetani, G.A., Grove, T.L., 1998. The influence of water on melting of mantle peridotite. *Contributions to Mineralogy and Petrology* 131, 323–346.
- Garrido, C.J., Bodinier, J.L., 1999. Diversity of mafic rocks in the Ronda peridotite: evidence for persuasive melt–rock reaction during heating of subcontinental lithosphere by upwelling asthenosphere. *Journal of Petrology* 40, 729–754.
- Ghiorso, M.S., Sack, R.O., 1995. Chemical mass-transfer in magmatic processes IV. A revised and internally consistent thermodynamic model for the interpolation and extrapolation of liquid–solid equilibria in magmatic systems at elevated-temperatures and pressures. *Contributions to Mineralogy and Petrology* 119 (2–3), 197–212.
- Green, D.H., 1973. Experimental melting studies on a model upper mantle composition at high pressure under water-saturated and water-undersaturated conditions. *Earth and Planetary Science Letters* 19, 37–53.
- Green, D.H., Ringwood, A.E., 1967. The genesis of basaltic magmas. *Contributions to Mineralogy and Petrology* 15 (2), 103–190.
- Grove, T.L., Kinzler, R.J., Bryan, B.W., 1992. Fractionation of mid-ocean ridge basalt (MORB). *Geophysical Monograph* 71, 281–310.
- Gudfinnsson, G.H., Presnall, D.C., 2000. Melting behaviour of model lherzolite in the system CaO–MgO–Al₂O₃–SiO₂–FeO. *Journal of Petrology* 41 (8), 1241–1269.
- Hanson, G.N., 1977. Geochemical evolution of the suboceanic mantle. *Journal of the Geological Society* 134 (2), 235–253.
- Hauri, E.H., 1996. Major-element variability in the Hawaiian mantle plume. *Nature* 382, 415–419.
- Hékinian, R., Juteau, T., Gràcia, E., Sichel, B., Sichel, S., Udintsev, G., Apprioual, R., Ligi, M., 2000. Submersible observations of Equatorial Atlantic mantle: The St Paul Fracture Zone region. *Marine Geophysical Researches* 21, 529–560.
- Helfrich, G., Wood, B.J., 2001. The Earth's mantle. *Nature* 412, 501–507.
- Herzberg, C., 2006. Petrology and thermal structure of the Hawaiian plume from Mauna Kea volcano. *Nature* 444, 605–609.
- Herzberg, C., 2011. Identification of source lithology in the Hawaiian and Canary Islands: implications for origins. *Journal of Petrology* 52 (1), 113–146.
- Herzberg, C., Asimow, P.D., 2008. Petrology of some oceanic island basalts: PRIMELT2.XSL software for primary magma calculation. *Geochemistry, Geophysics, Geosystems* 9 (Q09001). <http://dx.doi.org/10.1029/2008GC002057>.
- Herzberg, C., O'Hara, M.J., 2002. Plume-associated ultramafic magmas of Phanerozoic age. *Journal of Petrology* 43 (10), 1857–1883.
- Herzberg, C., Asimow, P.D., Arndt, N., Niu, Y., Leshner, C.M., Fitton, J.G., Cheadle, M.J., Saunders, A.D., 2007. Temperatures in ambient mantle and plumes: constraints from basalts, picrites, and komatiites. *Geochemistry, Geophysics, Geosystems* 8 (Q02006). <http://dx.doi.org/10.1029/2006GC001390>.
- Hirose, K., 1997. Partial melt compositions of carbonated peridotite at 3 GPa and role of CO₂ in alkali-basalt magma generation. *Geophysical Research Letters* 24 (22), 2837–2840.
- Hirose, K., Kushiro, I., 1993. Partial melting of dry peridotites at high pressures: determination of compositions of melts segregated from peridotite using aggregates of diamond. *Earth and Planetary Science Letters* 114 (4), 477–489.
- Hirschmann, M.M., Stolper, E.M., 1996. A possible role for garnet pyroxenite in the origin of the garnet signature in MORB. *Contributions to Mineralogy and Petrology* 124, 185–208.
- Hirschmann, M.M., Kogiso, T., Baker, M.B., Stolper, E.M., 2003. Alkalic magmas generated by partial melting of garnet pyroxenite. *Geology* 31 (6), 481–484.
- Ho, K.-s., Chen, J.-c., Smith, A.D., Juang, W.-s., 2000. Petrogenesis of two groups of pyroxenite from Tungchihsu, Penghu Islands, Taiwan Strait: implications for mantle metasomatism beneath SE China. *Chemical Geology* 167 (3–4), 355–372.
- Hofmann, A.W., 1997. Mantle geochemistry: the message from oceanic volcanism. *Nature* 385, 219–229.
- Hofmann, A.W., White, M.W., 1982. Mantle plumes from ancient oceanic crust. *Earth and Planetary Science Letters* 57, 421–436.
- Humphreys, E.M., Niu, Y., 2009. On the composition of ocean island basalts (OIB): the effects of lithospheric thickness variation and mantle metasomatism. *Lithos* 112, 118–136.
- Irving, A.J., Green, D.H., 2008. Phase relationships of hydrous alkalic magmas at high pressures: production of nepheline hawaiitic to mugearitic liquids by amphibole-dominated fractional crystallization within the lithospheric mantle. *Journal of Petrology* 49 (4), 741–756.
- Ito, G., Mahoney, J.J., 2005. Flow and melting of a heterogeneous mantle: 1. Method and importance to the geochemistry of ocean island and mid-ocean ridge basalts. *Earth and Planetary Science Letters* 230, 29–46.
- Jackson, J.M., Dasgupta, R., 2008. Compositions of HIMU, EM1, and EM2 from global trends between radiogenic isotopes and major elements in ocean island basalts. *Earth and Planetary Science Letters* 276, 175–186.
- Kelemen, P.B., Shimizu, N., Salters, V.J.M., 1995. Extraction of mid-ocean-ridge basalt from the upwelling mantle by focused flow of melt in dunite channels. *Nature* 375 (6534), 747–753.
- Kelemen, P.B., Hirth, G., Shimizu, N., Spiegelman, M., Dick, H.J.B., 1997. A review of melt migration processes in the adiabatically upwelling mantle beneath oceanic spreading ridges. *Philosophical Transactions of the Royal Society of London, Series A* 355, 283–318.

- Kelley, K.A., Plank, T., Grove, T.L., Stolper, E.M., 2006. Mantle melting as a function of water content beneath back-arc basins. *Journal of Geophysical Research* 111 (B09208).
- Keshav, S., Gudfinnsson, G.H., Sen, G., Fei, Y., 2004. High-pressure melting experiments on garnet clinopyroxene and the alkalic to tholeiitic transition in ocean-island basalts. *Earth and Planetary Science Letters* 223, 365–379.
- Kinzler, R.J., Grove, T.L., 1992a. Primary magmas of mid-ocean ridge basalts 1. Experiments and methods. *Journal of Geophysical Research* 97 (B5), 6885–6906.
- Kinzler, R.J., Grove, T.L., 1992b. Primary magmas of mid-ocean ridge basalts 2. Applications. *Journal of Geophysical Research* 97 (B5), 6907–6926.
- Klein, E.M., Langmuir, C.H., 1987. Global correlations of ocean ridge basalt chemistry with axial depth and crustal thickness. *Journal of Geophysical Research* 92 (B8), 8089–8115.
- Kogiso, T., Hirschmann, M.M., 2006. Partial melting experiments of bimineraleclogite and the role of recycled mafic oceanic crust in the genesis of ocean island basalts. *Earth and Planetary Science Letters* 249, 188–199.
- Kogiso, T., Hirose, K., Takahashi, E., 1998. Melting experiments on homogeneous mixtures of peridotite and basalt: application to the genesis of ocean island basalts. *Earth and Planetary Science Letters* 162, 45–61.
- Kogiso, T., Hirschmann, M.M., Frost, D.J., 2003. High-pressure partial melting of garnet pyroxenite: possible mafic lithologies in the source of ocean island basalts. *Earth and Planetary Science Letters* 216 (4), 603–617.
- Kogiso, T., Hirschmann, M.M., Pertermann, M., 2004a. High-pressure partial melting of mafic lithologies in the mantle. *Journal of Petrology* 45 (12), 2407–2422.
- Kogiso, T., Hirschmann, M.M., Reiners, P.W., 2004b. Length scales of mantle heterogeneities and their relationship to ocean island basalt geochemistry. *Geochimica et Cosmochimica Acta* 68 (2), 345–360.
- Korenaga, J., Kelemen, P.B., 2000. Major element heterogeneity in the mantle source of the North Atlantic igneous province. *Earth and Planetary Science Letters* 184, 251–268.
- Kushiro, I., 1969. The system forsterite–diopside–silica with and without water at high pressures. *American Journal of Science* 267 (A), 269–294.
- Kushiro, I., 1972. Effect of water on the composition of magmas formed at high pressures. *Journal of Petrology* 13, 311–334.
- Kushiro, I., 1975. On the nature of silicate melt and its significance in magma genesis: regularities in the shift of the liquidus boundaries involving olivine, pyroxene, and silica minerals. *American Journal of Science* 275, 411–431.
- Kushiro, I., 1996. Partial melting of a fertile mantle peridotite at high pressures: an experimental study using aggregates of diamond. In: Basu, A., Hart, S.R. (Eds.), *Earth Processes: Reading the Isotopic Code: Geophysical Monograph*, pp. 109–122.
- Kushiro, I., Yoder, H.S., 1974. Formation of eclogite from garnet lherzolite: liquidus relations in a portion of the system $MgSiO_3$ – $CaSiO_3$ – Al_2O_3 at high pressures. *Carnegie Institution of Washington, Yearbook*, 73, 266–269.
- Lambart, S., Laporte, D., Schiano, P., 2009. An experimental study of pyroxenite partial melts at 1 and 1.5 GPa: implications for the major-element composition of mid-ocean ridge basalts. *Earth and Planetary Science Letters* 288 (1–2), 335–347.
- Lambart, S., Laporte, D., Provost, A., Schiano, P., 2012. Fate of pyroxenite-derived melts in the peridotitic mantle: thermodynamical and experimental constraints. *Journal of Petrology* 53 (3), 451–476.
- Langmuir, C.H., Klein, E.M., Plank, T., 1992. Petrological systematics of mid-ocean ridge basalts: constraints on melt generation beneath ocean ridges. *American Geophysical Union Monograph* 71, 183–280.
- Laporte, D., Toplis, M.J., Seyler, M., Devidal, J.-L., 2004. A new experimental technique for extracting liquids from peridotite at very low degrees of melting: application to partial melting of depleted peridotite. *Contributions to Mineralogy and Petrology* 146 (4), 463–484.
- Laske, G., Phipps Morgan, J., Orcutt, J.A., 1999. First results from the Hawaiian swell experiment. *Geophysical Research Letters* 26, 3397–3400.
- Laubier, M., Schiano, P., Doucelance, R., Ottolini, L., Laporte, D., 2007. Olivine-hosted melt inclusions and melting processes beneath the FAMOUS zone (Mid-Atlantic Ridge). *Chemical Geology* 240, 129–150.
- Le Bas, M.J., 1989. Nephelinitic and basanitic rocks. *Journal of Petrology* 30, 1299–1312.
- Le Roux, P.J., Le Roex, A.P., Schilling, J.-G., Shimizu, N., Perkins, W.W., Pearce, N.J.G., 2002. Mantle heterogeneity beneath the southern Mid-Atlantic Ridge: trace element evidence for contamination of ambient asthenospheric mantle. *Earth and Planetary Science Letters* 203 (1), 479–498.
- Lee, C.-T.A., Luffi, P., Plank, T., Dalton, H., Leeman, W.P., 2009. Constraints on the depths and temperatures of basaltic magma generation on Earth and other terrestrial planets using new thermobarometers for mafic magmas. *Earth and Planetary Science Letters* 279, 20–33.
- Liu, X., O'Neill, H.C.S., 2004a. The effect of Cr_2O_3 on the partial melting of spinel lherzolite in the system CaO – MgO – Al_2O_3 – SiO_2 – Cr_2O_3 at 1.1 GPa. *Journal of Petrology* 45 (11), 2261–2286.
- Liu, X., O'Neill, H.C.S., 2004b. Partial melting of spinel lherzolite in the system CaO – MgO – Al_2O_3 – SiO_2 – K_2O at 1.1 GPa. *Journal of Petrology* 45 (7), 1339–1368.
- Liu, X., O'Neill, H.C.S., 2007. Effects of P_2O_5 and TiO_2 on the partial melting of spinel lherzolite in the system CaO – MgO – Al_2O_3 – SiO_2 at 1.1 GPa. *The Canadian Mineralogist* 45, 649–655.
- Liu, X., Presnall, D.C., 2000. Liquidus phase relations in the system CaO – MgO – Al_2O_3 – SiO_2 at 2.0 GPa: applications to basalt formation, eclogites, and igneous sapphirine. *Journal of Petrology* 41, 3–20.
- Maaloe, S., Wyllie, P.J., 1979. The join grossularite–pyrope at 30 kbar and its petrological significance. *American Journal of Science* 279, 288–301.
- Maaloe, S., James, D., Smedley, P., Petersen, S., Garmann, L.B., 1992. The Koloa Volcanic Suite of Kauai, Hawaii. *Journal of Petrology* 33 (4), 761–784.
- Macdonald, G.A., Katsura, T., 1964. Chemical composition of Hawaiian lavas. *Journal of Petrology* 5 (1), 82–133.
- Mallik, A., Dasgupta, R., 2012. Reaction between MORB-eclogite derived melts and fertile peridotite and generation of ocean island basalts. *Earth and Planetary Science Letters* 329–330, 97–108.
- Marchesi, C., Garrido, C.J., Bosch, D., Bodinier, J.L., Gervilla, F., 2011. Mantle refertilization by garnet pyroxenite melts: evidence from the Ronda peridotite massif, southern Spain. *American Geophysical Union, Fall Meeting* 2011, San Francisco, USA.
- Mazzucchelli, M., Rivalenti, G., Brunelli, D., Zanetti, A., Boari, E., 2009. Formation of highly refractory dunite by focused percolation of pyroxenite-derived melt in the Balmuccia peridotite massif (Italy). *Journal of Petrology* 50 (7), 1205–1233.
- McKenzie, D., Bickle, M.J., 1988. The volume and composition of melt generated by extension of the lithosphere. *Journal of Petrology* 29 (3), 625–679.
- McKenzie, D., O'Nions, R.K., 1991. Partial melt distributions from inversion of rare earth element concentrations. *Journal of Petrology* 32 (5), 1021–1091.
- Médard, E., Schmidt, M.W., Schiano, P., Ottolini, L., 2006. Melting of amphibole-bearing wehrlites: an experimental study on the origin of ultra-calcic nepheline-normative melts. *Journal of Petrology* 47 (3), 481–504.
- Melson, W.G., O'Hearn, T., 2003. Smithsonian volcanic glass file. *Petrological Database of the Ocean Floor*.
- Michael, P.J., 1988. The concentration, behaviour and storage of H_2O in the suboceanic upper mantle: implications for mantle metasomatism. *Geochimica et Cosmochimica Acta* 52, 555–566.
- Michael, P.J., Langmuir, C.H., Dick, H.J.B., Snow, J.E., Goldstein, S.L., Graham, D.W., Lehnert, K., Kurras, G., Jokar, W., Mühe, R., Edmonds, H.N., 2003. Magmatic and amagmatic seafloor generation at the ultraslow-spreading Gakkel ridge, Arctic Ocean. *Nature* 423, 956–961.
- Milholland, C.S., Presnall, D.C., 1998. Liquidus phase relations in the CaO – MgO – Al_2O_3 – SiO_2 system at 3.0 GPa: the aluminous pyroxene thermal divide and high-pressure fractionation of picritic and komatiitic magmas. *Journal of Petrology* 39 (1), 3–27.
- Moine, B.N., Cottin, J.-Y., Sheppard, S.M.F., Grégoire, M., O'Reilly, S.Y., Giret, A., 2000. Incompatible trace element and isotopic (D/H) characteristics of amphibole- and phlogopite-bearing ultramafic to mafic xenoliths from Kerguelen Islands (TAAF, South Indian Ocean). *European Journal of Mineralogy* 12 (4), 761–777.
- Moore, J.G., Clague, D., 1992. Volcano growth and evolution of island of Hawaii. *Geological Society of America Bulletin* 104, 1471–1494.
- Mysen, B.O., Ryerson, F.J., Virgo, D., 1980. The influence of TiO_2 on the structure and derivative properties of silicate melts. *American Mineralogist* 65, 1150–1165.
- Neumann, E.-R., Marti, J., Mitjavila, J., Wulff-Pedersen, E., 1999. Origin and implications of mafic xenoliths associated with Cenozoic extension-related volcanism in the Valencia Trough, NE Spain. *Mineralogy and Petrology* 65, 113–139.
- Nicholls, I.A., Ringwood, A.E., 1973. Effect of water on olivine stability in tholeiites and production of silica-saturated magmas in the island arc environment. *Journal of Petrology* 81, 285–306.
- Niu, Y.-L., Batiza, R., 1997. Trace element evidence from seamounts for recycled oceanic crust in the Eastern Pacific mantle. *Earth and Planetary Science Letters* 148 (3–4), 471–483.
- Niu, Y.L., Collerson, K.D., Batiza, R., Wendt, J.J., Regelous, M., 1999. Origin of enriched-type mid-ocean ridge basalt at ridges far from mantle plumes: the East Pacific Rise at $11^{\circ}20'N$. *Journal of Geophysical Research* 104 (B4), 7067–7087.
- Niu, Y.-L., Regelous, M., Wendt, J., Batiza, R., O'Hara, M.J., 2002. Geochemistry of near-EPR seamounts: importance of source vs. process and the origin of enriched mantle component. *Earth and Planetary Science Letters* 199, 327–345.
- Niu, Y.L., Wilson, M., Humphreys, E.M., O'Hara, M.J., 2011. The origin of intra-plate ocean island basalts (OIB): the lid effect and its geodynamic implications. *Journal of Petrology* 52 (7–8), 1443–1468.
- O'Hara, M.J., 1965. Primary magmas and the origin of basalts. *Scottish Journal of Geology* 1, 19–40.
- O'Hara, M.J., 1968. The bearing of phase equilibria studies in synthetic and natural systems on the origin and evolution of basic and ultrabasic rocks. *Earth-Science Reviews* 4, 69–133.
- O'Hara, M.J., 1969a. The relationship between liquid and crystals in univariant equilibria of four component systems, their application to the origin and melting of ultramafic rocks and refractories. *Progress in Experimental Petrology, First Report, NERC Supported Research Units in British Universities, 1965–1968*, pp. 114–120.
- O'Hara, M.J., 1969b. Quaternary invariant equilibria involving liquid; their application to the origin of mafic and ultramafic nodules in igneous rocks. *Progress in Experimental Petrology, First Report, NERC Supported Research Units in British Universities, 1965–1968*, pp. 120–128.
- O'Hara, M.J., 1972. Data reduction and projection schemes for complex compositions. In: Eam, U. (Ed.), *Progress in Experimental Petrology*. NERC, Manchester, Edinburgh, pp. 103–126.
- O'Hara, M.J., Yoder, H.S., 1963. Partial melting of the mantle. *Carnegie Institution of Washington, Yearbook*, 62, pp. 66–71.
- O'Hara, M.J., Yoder, H.S., 1967. Formation and fractionation of basic magmas at high pressures. *Scottish Journal of Geology* 3, 67–117.
- Orejana, D., Villaseca, C., Paterson, B.A., 2006. Geochemistry of pyroxenitic and hornblende xenoliths in alkaline lamprophyres from the Spanish Central System. *Lithos* 86, 167–196.
- Parman, S.W., Grove, T.L., 2004. Harzburgite melting with and without H_2O : experimental data and predictive modeling. *Journal of Geophysical Research* 109 (B2). <http://dx.doi.org/10.1029/2003jb002566>.
- Pertermann, M., Hirschmann, M.M., 2003. Anhydrous partial melting experiments on MORB-like eclogite: phase relations, phase compositions and mineral–melt partitioning of major elements at 2–3 GPa. *Journal of Petrology* 44 (12), 2173–2201.
- Phipps Morgan, J., 2001. Thermodynamics of pressure release melting of a veined plum pudding mantle. *Geochemistry, Geophysics, Geosystems* 2 (4). <http://dx.doi.org/10.1029/2000GC000049>.

- Pilet, S., Hernandez, J., Sylvestre, P., Poujol, M., 2005. The metasomatic alternative for ocean island basalt chemical heterogeneity. *Earth and Planetary Science Letters* 236, 148–166.
- Pilet, S., Baker, M.B., Stolper, E.M., 2008. Metasomatized lithosphere and the origin of alkaline lavas. *Science* 320, 916.
- Pilet, S., Ulmer, P., Villiger, S., 2010. Liquid line of descent of a basanitic liquid at 1.5 GPa: constraints on the formation of metasomatic veins. *Contributions to Mineralogy and Petrology* 159 (5), 621–643.
- Pilet, S., Baker, M.B., Müntener, O., Stolper, E.M., 2011. Monte Carlo simulations of metasomatic enrichment in the lithosphere and implications for the source of alkaline basalts. *Journal of Petrology* 52 (7–8), 1415–1442.
- Plank, T., Langmuir, C.H., 1992. Effects of the melting regime on the composition of the oceanic crust. *Journal of Geophysical Research* 97 (B13), 19749–19770.
- Porreca, C., Selverstone, J., Samuels, K., 2006. Pyroxenite xenoliths from the Rio Puerco volcanic field, New Mexico: melt metasomatism at the margin of the Rio Grande rift. *Geosphere* 2 (7), 333–351.
- Presnall, D.C., Dixon, S.A., Dixon, J.R., O'Donnell, T.H., Brenner, N.L., Schrock, R.L., Dycus, D.W., 1978. Liquidus phase relations on the join diopside–forsterite–anorthite at 1 atm to 20 kbar; their bearing on the generation and crystallization of basaltic magma. *Contributions to Mineralogy and Petrology* 66, 203–220.
- Presnall, D.C., Gudfinnsson, G.H., Walter, M.J., 2002. Generation of mid-ocean ridge basalts at pressure from 1 to 7 GPa. *Geochimica et Cosmochimica Acta* 66, 2073–2090.
- Prytulak, J., Elliott, T., 2007. TiO₂ enrichment in ocean island basalts. *Earth and Planetary Science Letters* 263, 388–403.
- Putirka, K.D., Johnson, M., Kinzler, R.J., Walker, D., 1996. Thermobarometry of mafic igneous rocks based on clinopyroxene–liquid equilibria, 0–30 kbar. *Contributions to Mineralogy and Petrology* 123, 92–108.
- Putirka, K.D., Ryerson, F.J., Mikaelian, H., 2003. New igneous thermobarometers for mafic and evolved lava compositions, based on clinopyroxene + liquid equilibria. *American Mineralogist* 88, 1542–1554.
- Robinson, J.A.C., Wood, B.J., Blundy, J.D., 1998. The beginning of melting of fertile and depleted peridotite at 1.5 GPa. *Earth and Planetary Science Letters* 155 (1–2), 97–111.
- Saal, A.E., Hauri, E., Langmuir, C.H., Perfit, M.R., 2002. Vapour undersaturation in primitive mid-ocean-ridge basalt and the volatile content of Earth's upper mantle. *Nature* 419, 451–455.
- Salters, V.J.M., Dick, H.J.B., 2002. Mineralogy of the mid-ocean-ridge basalt source from neodymium isotopic composition of abyssal peridotites. *Nature* 418 (6893), 68–72.
- Schiano, P., Birck, J.-L., Allègre, C.J., 1997. Osmium–strontium–neodymium–lead isotopic covariations in mid-ocean ridge basalt glasses and the heterogeneity of the upper mantle. *Earth and Planetary Science Letters* 150 (3–4), 363–379.
- Schiano, P., Eiler, J.M., Hutcheon, I.D., Stolper, E.M., 2000. Primitive CaO-rich, silica-undersaturated melts in island arcs: evidence for the involvement of clinopyroxene-rich lithologies in the petrogenesis of arc magmas. *Geochemistry, Geophysics, Geosystems* 1 (5) (paper number 1999GC000032).
- Sen, I.S., Bizimis, M., Sen, G., Huang, S., 2011. A radiogenic Os component in the oceanic lithosphere? Constraints from Hawaiian pyroxenite xenoliths. *Geochimica et Cosmochimica Acta* 75 (17), 4899–4916.
- Seyler, M., Cannat, M., Mével, C., 2003. Evidence for major-element heterogeneity in the mantle source of abyssal peridotites from the Southwest Indian Ridge (52° to 68° E). *Geochemistry, Geophysics, Geosystems* 4 (2). <http://dx.doi.org/10.1029/2002GC000305>.
- Seyler, M., Lorand, J.-P., Toplis, M.J., Godard, G., 2004. Asthenospheric metasomatism beneath the mid-ocean ridge: evidence from depleted abyssal peridotites. *Geology* 32 (2), 301–304.
- Shorttle, O., MacLennan, J., 2011. Compositional trends of Icelandic basalts: implications for short-length scale lithological heterogeneity in mantle plumes. *Geochemistry, Geophysics, Geosystems* 12 (Q11008). <http://dx.doi.org/10.1029/2011GC003748>.
- Sleep, N.H., 1984. Tapping of magmas from ubiquitous mantle heterogeneities: an alternative to mantle plumes. *Journal of Geophysical Research* 89, 10029–10041.
- Sleep, N.H., 1990. Hotspots and mantle plumes: some phenomenology. *Journal of Geophysical Research* 95 (B5), 6715–6736.
- Sobolev, A.V., Hofmann, A.W., Nikogosian, I.K., 2000. Recycled oceanic crust observed in ghost plagioclase within the source of Mauna Loa lavas. *Nature* 404, 986–989.
- Sobolev, A.V., Hofmann, A.W., Sobolev, S.V., Nikogosian, I.K., 2005. An olivine-free mantle source of Hawaiian shield basalts. *Nature* 434, 590–597.
- Sobolev, A.V., Hofmann, A.W., Kuzmin, D.V., Yaxley, G.M., Arndt, N.T., Chung, S.-L., Danyushevsky, L.V., Elliott, T., Frey, F.A., Garcia, M.O., Gurenko, A.A., Kamenetsky, V.S., Kerr, A.C., Krivolutskaia, N.A., Matvienkov, V.V., Nikogosian, I.K., Rocholl, A., Sigurdsson, I.A., Sushchevskaya, N.M., Teklay, M., 2007. The amount of recycled crust in sources of mantle-derived melts. *Science* 316 (5823), 412–417.
- Spandler, C., Yaxley, G., Green, D.H., Rosenthal, A., 2008. Phase relations and melting of anhydrous K-bearing eclogite from 1200 to 1600°C and 3 to 5 GPa. *Journal of Petrology* 49 (4), 771–795.
- Stolper, E.M., 1980. A phase diagram for mid-ocean ridge basalts: preliminary results and implications for petrogenesis. *Contributions to Mineralogy and Petrology* 74 (1), 13–27.
- Stolper, E.M., Asimow, P.D., 2007. Insights into mantle melting from graphical analysis of one-component systems. *American Journal of Science* 307, 1051–1139.
- Stolper, E.M., Sherman, S., Garcia, M., Baker, M.B., Seaman, C., 2004. Glass in the submarine section of the HSDP2 drill core, Hilo, Hawaii. *Geochemistry, Geophysics, Geosystems* 5 (7), Q07G15. <http://dx.doi.org/10.1029/2003GC000553>.
- Stracke, A., Bourdon, B., 2009. The importance of melt extraction for tracing mantle heterogeneity. *Geochimica et Cosmochimica Acta* 73, 218–238.
- Stracke, A., Salters, V.J.M., Sims, K.W.W., 1999. Assessing the presence of garnet–pyroxenite in the mantle sources of basalts through combined hafnium–neodymium–thorium isotope systematics. *Geochemistry, Geophysics, Geosystems* 1 (12), 1–13.
- Suhr, G., Kelemen, P., Paulick, H., 2008. Microstructures in Hole 1274A peridotites, ODP Leg 209, Mid-Atlantic Ridge: tracking the fate of melts percolating in peridotite as the lithosphere is intercepted. *Geochemistry, Geophysics, Geosystems* 9 (3), Q03012. <http://dx.doi.org/10.1029/2007GC001726>.
- Takahashi, E., 1986. Melting of a dry peridotite KBL-1 up to 14 GPa: implications on the origin of peridotitic upper mantle. *Journal of Geophysical Research* 91 (B9), 9367–9382.
- Takahashi, E., Kushiro, I., 1983. Melting of a dry peridotite at high pressures and basalt magma genesis. *Earth and Planetary Science Letters* 162, 63–80.
- Takahashi, E., Nakajima, K., Wright, T.L., 1998. Origin of the Columbia River basalts: melting model of a heterogeneous plume head. *Earth and Planetary Science Letters* 162, 63–80.
- Walker, D., Shibata, T., DeLong, S., 1979. Abyssal tholeiites from the Oceanographer Fracture Zone. *Contributions to Mineralogy and Petrology* 70 (2), 111–125.
- Walter, M.J., 1998. Melting of garnet peridotite and the origin of komatiite and depleted lithosphere. *Journal of Petrology* 39 (1), 29–60.
- Walter, M.J., Presnall, D.C., 1994. Melting behaviour of simplified lherzolite in the system CaO–MgO–Al₂O₃–SiO₂–Na₂O from 7 to 35 kbar. *Journal of Petrology* 35, 329–359.
- Warren, J.M., Shimizu, N., 2010. Cryptic variations in abyssal peridotite compositions: evidence for shallow-level melt infiltration in the oceanic lithosphere. *Journal of Petrology* 51 (1–2), 395–423.
- Wasylenko, L.E., Baker, M.B., Kent, A.J.R., Stolper, E.M., 2003. Near-solidus melting of the shallow upper mantle: partial melting experiments on depleted peridotite. *Journal of Petrology* 44 (7), 1163–1191.
- White, W.M., 1985. Sources of oceanic basalts: radiogenic isotopic evidence. *Geology* 13, 115–118.
- Wiens, D.A., Kelley, K.A., Plank, T., 2006. Mantle temperature variations beneath back-arc spreading centers inferred from seismology, petrology, and bathymetry. *Earth and Planetary Science Letters* 248, 30–42.
- Wood, D.A., 1979. A variably veined suboceanic upper mantle-genetic significance for mid-ocean ridge basalts from geochemical evidence. *Geology* 7, 499–503.
- Wood, M.I., Hess, P.C., 1980. The structural role of Al₂O₃ and TiO₂ in immiscible silicate liquids in the system SiO₂–MgO–CaO–FeO–TiO₂–Al₂O₃. *Contributions to Mineralogy and Petrology* 72, 319–328.
- Yasuda, A., Fujii, T., Kurita, K., 1994. Melting phase relations of an anhydrous mid-ocean ridge basalt from 3 to 20 GPa: implications for the behavior of subducted oceanic crust in the mantle. *Journal of Geophysical Research* 99 (B5), 9401–9414.
- Yaxley, G.M., Brey, G.P., 2004. Phase relations of carbonate-bearing eclogite assemblages from 2.5 to 5.5 GPa: implications for petrogenesis of carbonatites. *Contributions to Mineralogy and Petrology* 146, 606–619.
- Yaxley, G.M., Green, D.H., 1998. Reactions between eclogite and peridotite: mantle refertilisation by subduction of oceanic crust. *Schweizerische mineralogische und petrographische Mitteilungen* 78, 243–255.
- Yaxley, G.M., Sobolev, A.V., 2007. High-pressure partial melting of gabbro and its role in the Hawaiian magma source. *Contributions to Mineralogy and Petrology* 154, 371–383.
- Yoder, H.S., Tilley, C.E., 1962. Origin of basalt magmas: an experimental study of natural and synthetic rock systems. *Journal of Petrology* 3 (3), 342–532.
- Zhang, G., 2011. Comparative study of magmatism in East Pacific Rise versus nearby seamounts: constraints on magma supply and thermal structure beneath mid-ocean ridge. *Acta Geologica Sinica* 85 (6), 1286–1298.
- Zindler, A., Hart, S.R., 1986. Chemical geodynamics. *Annual Review of Earth and Planetary Sciences* 14, 493–571.
- Zindler, A., Staudigel, H., Batiza, R., 1984. Isotope and trace element geochemistry of young Pacific seamounts: implications for the scale of upper mantle heterogeneity. *Earth and Planetary Science Letters* 70, 175–195.